Journal of Cultural Heritage 77 (2026) 67–80

Contents lists available at ScienceDirect

Journal of Cultural Heritage

journal homepage: www.elsevier.com/locate/culher

Original article

# The key role of Pb-Bi, Pb-Te-Se and S-Fe-Te-Se inclusions, microstructures, and corrosion processes in reconstructing Etruscan metallurgy at Pyrgi (Latium, Italy)

Marta Porcaro[a], Laura M. Michetti[b], Alessandro Conti[b], Giacomo Mazzotta[a], Tilde de Caro[c], Matteo Paciucci[d], Antonio Doménech-Carbó[e], Caterina De Vito[a,*]

[a] Department of Earth Sciences, Sapienza University of Rome, P.le Aldo Moro 5, 00185 Rome, Italy
[b] Department of Classics, Sapienza University of Rome, P.le Aldo Moro 5, 00185 Rome, Italy
[c] Institute for the Study of Nanostructured Materials, National Research Council (ISMN-CNR), Provincial Road 35 d, No. 9-00010 Montelibretti, 00010 Rome, Italy
[d] Institute of Environmental Geology and Geoengineering, National Research Council of Italy (CNR IGAG), Research Area of Rome 1, 00010 Rome, Italy
[e] Department of Analytical Chemistry, University of Valencia, Dr. Moliner 50, 46100 Burjassot, Valencia, Spain

## ARTICLE INFO

*Article history:*
Received 24 April 2025
Accepted 26 October 2025

*Keywords:*
Tellurium-selenium inclusions
Microstructures
Lead-bismuth
Etruscan copper production

## ABSTRACT

The archaeological site of Pyrgi (Santa Severa, Rome, Italy) has yielded a diverse range of metal artifacts that provide valuable insights into the Etruscans' metallurgical knowledge and material selection practices. This study focuses on micro-inclusions, microstructure, chemical composition, and corrosive process of arrowheads, nails, and *aes rude*. Scanning Electron Microscopy with Energy Dispersive Spectroscopy (SEM-EDS), micro-Raman spectroscopy, and electrochemical analysis, *i.e.*, Voltammetry of Immobilized Particles (VIMP), and Mott-Schottky (MS) were used. The nails and *aes rude* are pure copper, with minor contents of tin and lead, while the arrowheads are ternary bronze alloy (Cu-Sn-Pb). The microstructures of nails and *aes rude* are characterized by the presence of Pb-Bi, Pb-Te-Se, and S-Te-Se-Fe micro-inclusions within the metal matrix, which provide insights into smelting processes, the nature of the ores used, and technological capabilities. The variability of inclusions suggests the use of polymetallic minerals as starting materials. Tellurium and selenium suggest refining practices and smelting techniques that were not fully optimized. The corrosion patinas are composed of cuprite, malachite, and trihydroxychlorides. The Mott-Schottky analysis highlighted variations in the electrochemical response of the corrosion layers, suggesting different alteration conditions among areas of Pyrgi. These results contribute to the exploration of Etruscan metallurgical choices and techniques, highlighting variations in smelting processes, raw materials, and processing practices.

## 1. Introduction and aim

The site of Pyrgi (Santa Severa, Italy) was the harbor of Caere, an important city of ancient Etruria. It is located along the Tyrrhenian coast of central Italy and represents one of the main Etruscan ports from the late 7th century BC. The settlement, excavated by Sapienza University of Rome since 1957, was known for its large sanctuaries. The Greek literature reports the frequentation of Pyrgi by Greek and Phoenician merchants [1]. Two temples with architectural terracotta decorations characterized the Monumental Sanctuary. The metallic and ceramic artifacts found at this site testify to the predominant role of the Etruscans in commerce and religion.

This research is focused on twelve metal artifacts, including arrowheads, nails, and "*aes rude*," a primitive form of a coin [2,3]. Nails as cultural heritage objects have less value than other artifacts, but they play an important role in understanding technological development by providing information on metallurgical techniques employed [4,5]. Arrowheads provided insights into the offensive use of metals, allowing for a better understanding of material choices, aiming to maximize performance and meet specific functional requirements [6–8]. *Aes rude* was the earliest form of proto-coin, in which the value of the metal was intrinsically linked to its role as a raw material [2]. Unlike the symbolic value associated with minted coins that emerged in later periods, *aes rude* de-

---

* Corresponding author.
*E-mail address:* caterina.devito@uniroma1.it (C. De Vito).

https://doi.org/10.1016/j.culher.2025.10.021

rived its value directly from the material itself. They are irregular in shape, rough pieces of metal made of copper or bronze, lacking engravings or marks, and used as a medium of exchange, hoarding, and votive offerings [9]. Non-standardized shape and heterogeneous chemical composition suggest that they were produced with less care than coins produced later [2], which is useful for understanding the Etruscan economy and reconstructing the exchange patterns of these people.

The aim is to investigate inclusions, microstructure, manufacturing techniques, and corrosion processes occurring during burial conditions. The presence of selenium (Se) and tellurium (Te) in several samples reveals information on ancient metallurgical practices. Additionally, the study of inclusions provides insights into the nature of ores and smelting methods [10–13].

As recently reported [14], the hydrothermal ore systems are responsible for the formation of nano to micron-scale polymetallic inclusions (Ag-Au-Cu-Pb(-Fe-Zn)-As-Sb-S-Se). This process appears to be related to the coalescence of nano and micro-melt precursors during the transport from the geological source to the site of mineral deposition, where they play a key role in metal mineralization. The variability and composition of inclusions observed in Etruscan samples may reflect the use of polymetallic ores of similar geological origin [14]. This comparison highlights that selenium and tellurium in our materials are not accidental contaminants, but potential markers of the raw ores and metallurgical processes employed. These trace elements are documented in mining geology and industry [15–20], but they are rarely analyzed and discussed in archaeometallurgical studies [10,21–23]. Their association with sulfur (S), iron (Fe), copper (Cu), lead (Pb), and bismuth (Bi) may reveal specific aspects of the metallurgical skills of the Etruscans. In addition, the research will verify whether the *aes rude* were recasting to produce new objects, such as nails, and to understand the production cycles and reuse of the alloys.

Scanning electron microscopy with energy dispersive spectroscopy (SEM-EDS) was used to explore the artifacts' morphology and chemical composition. EDS provided semi-quantitative chemical analysis and elemental mappings of the investigated areas of the samples. Micro-Raman spectroscopy provided information on the compounds occurring in the corrosion layers of the artifacts. Voltammetry of immobilized particles (VIMP) and Mott-Schottky (MS) analysis are used to examine the electrochemical properties of materials, providing insight into corrosion and degradation processes.

The results may contribute to expanding knowledge of how this population managed resources, attributed values to objects, and exploited metal as a key element of their cultural and technological heritage.

## 2. Archaeological context

The harbor and sanctuary of Pyrgi played a crucial role in the history of the ancient Mediterranean (Fig. 1). It served as the maritime gateway of Caere (modern-day Cerveteri, RM), whose wealth was built on controlling maritime trade[1]. The sanctuary consists of two sacred areas, separated by a river [24].

The Monumental Sanctuary, featuring two large temples (A and B) built between the late 6th and mid-5th centuries B.C. and dedicated to Uni and Leucothea, is considered an expression of Caere's political power.

The Southern Sanctuary is an independent sacred area, lacking monumental architecture and characterized by numerous small altars and modest structures. Its layout, rituals, types of votive offerings, and inscribed dedications suggest the practice of Demeter-related cults. Many Etruscan inscriptions indicate the parallel worship of Cavatha and her underworld companion Śur/Śuri.

The public-ceremonial quarter lies between the sanctuary and the settlement. The layout of its buildings and distinctive finds suggest that this area functioned as a residential quarter with ceremonial purposes, including customs operations and manufacturing activities both to the port and the sanctuary [25,26].

Recent studies have also suggested the presence of a metallurgical production area, providing evidence of in situ manufacturing of tools (see S.1, Supplementary Materials).

The geological and sedimentary context of the site is provided in the Supplementary Materials (see S.2).

## 3. Materials and methods

### 3.1. Materials

Twelve copper and copper-based alloy artifacts, including six nails, three *aes rude*, and three arrowheads (Fig. 2A-L), were selected for this study based on typology, representativeness, and provenance, to achieve diversification of the discovery area within the site and chronology (Table 1).

Eleven samples were cut to obtain cross-sections that allowed exploration of the layers from the outer surface to the core. Only nail 04BV57 (Fig. 2E) was kept intact, as it is one of the few small-sized samples found in relatively good condition. It was nonetheless included in the set of analyzed artefacts since, together with sample 49,466 (Fig. 2A), it is the only other small nail, allowing for the assessment of possible affinities or differences between morphology and composition.

### 3.2. Methods

Scanning electron microscopy (SEM-EDS) was used to characterize the microstructures and chemical composition of the artefacts. The EDS microanalysis system enables the acquisition of elemental composition and mapping of the distribution of elements in samples.

Micro-Raman analysis and electrochemical investigations were chosen to study the corrosion of the artifacts. Micro-Raman spectroscopy was used to characterize surface corrosion products and inner zone phases. The interpretation of the spectra was performed by comparing them with the RRUFF reference database. Voltammetry of immobilized microparticles (VIMP) was useful for understanding corrosion processes and determining the state of preservation of the artifacts [27,28]. Mott-Schottky (MS) analysis is used to characterize the semiconducting properties of the corrosion products forming on metal surfaces [29,30].

Information on instruments and measurement parameters can be found in S.3, Supplementary Materials.

## 4. Results

### 4.1. Characterization of microstructures, chemical composition and entrapped inclusions in the metallic matrix

#### 4.1.1. The nails

All nails are composed of pure copper (Cu), with minor amounts of tin (Sn) and lead (Pb) (Table S.1, Supplementary Materials). The abundance of Pb globules and their distribution within the matrix permitted discrimination among the nails. The inclusions of 2–10 µm in size are essentially of two types, *i.e.,* Pb-rich globules with Bi and S-rich globules with Cu and Fe. EDS analyses showed the presence of inclusions containing tellurium (Te) and selenium (Se), associated mainly with sulfur globules, and in nails 9787 and 49,466 also with lead globules (Fig. 3 and Fig. S.1). Only nail 52,640 showed globular inclusions (5–10 µm), enriched in copper, sulfur and iron, irregularly arranged, having elon-

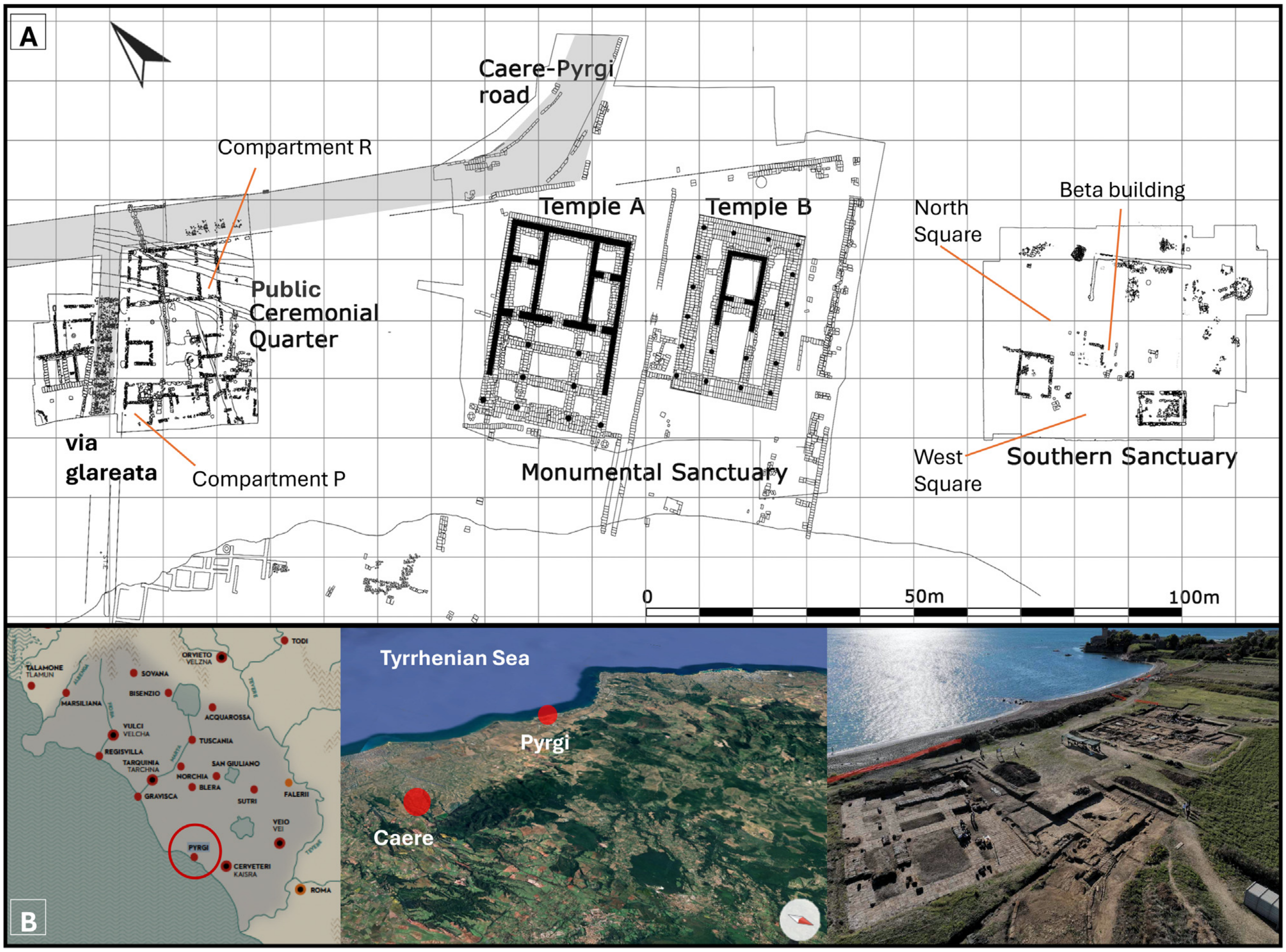

**Fig. 1.** Planimetry of the Pyrgi archaeological site: (A) topography and (B) geographical context.

**Table 1**
Information on the twelve artifacts analyzed in the study. The table reports the Inventory Number, type, finding area, period, and reference image in Fig. 2.

| Inventory No. | Typology | Provenance | Period | Image |
|---|---|---|---|---|
| 49,466 | Nail, square section | Monumental Sanctuary | 5th - 4th century B.C. | A |
| 9787 | Nail stem, circular section | Monumental Sanctuary, Temple A | First half of the 5th century B.C. | B |
| 52,640 | Nail, square section | Monumental Sanctuary, Temple B | End of the 6th century B.C. | C |
| 58,257 | Nail, square section | Monumental Sanctuary, Temple A | First half of the 5th century B.C. | D |
| 04BV57 | Nail, circular section | Southern Sanctuary, beta building | 5th - 4th century B.C. | E |
| 04BG78 | Nail stem, square section | Southern Sanctuary, West Square | 5th - 4th century B.C. | F |
| 99BA28 | *Aes rude* | Southern Sanctuary, North Square | 5th - 4th century B.C. | G |
| P18.1290.3 | *Aes rude* | Compartment R, "public ceremonial" Quarter | 6th - 5th century B.C. | H |
| 07AD4 | *Aes rude* | Southern Sanctuary, West Square | 5th - 4th century B.C. | I |
| 02BP48 | Three-winged arrowhead | Monumental Sanctuary | 5th - 4th century B.C. | J |
| P18.1202.100 | Two-winged arrowhead | Compartment P, "public ceremonial" Quarter | 6th - 5th century B.C. | K |
| 81.1098 | Three-winged arrowhead | Monumental Sanctuary, a square in front of the temples | 5th - 3rd century B.C. | L |

gated shapes according to a preferential direction (Fig. S.2b). Lead globules were found in almost all the nails, except nail 04BG78. Find 9787 had the widest and most uniform distribution of Pb-rich globules within the matrix (Fig. S.2c).

The nail 49,466 is a bronze alloy with an Sn concentration of around 2 %, showing a uniform microstructure, with slight compositional variations at the microscopic level and small Pb globules (Fig. S.2d and S.3). In the inner part of the sample, the compositional variations did not follow a precise direction, whereas toward the outside the branching became more evident, taking on a "banded" appearance. This variation is due to the presence of two phases, *i.e.*, pure copper (phase A, dark gray) and copper and tin (phase B, lighter grey), whose distribution was influenced by the dendritic microstructure (Fig. S.2d). Phase B has an average composition of 97.8 wt% Cu and 2.2 wt% Sn. The chemical composition and microstructures of the corrosion-prone areas showed that the patina, enriched in O and Cl (Table S.1), followed the "banded" distribution, progressing preferentially along phase A towards the core (Fig. S.3). This behavior is due to the lower resistance of Cu at the corrosion than the Cu–Sn solid solution of phase B.

Finally, nail 04BV57, the only unsampled find, was analysed using EDS spectra and surface X-ray mapping. The results revealed the presence of Cu and the complete absence of Sn. Exogenous elements from the burial soil, such as Si, Al, Fe, S, and Cl, were also found.

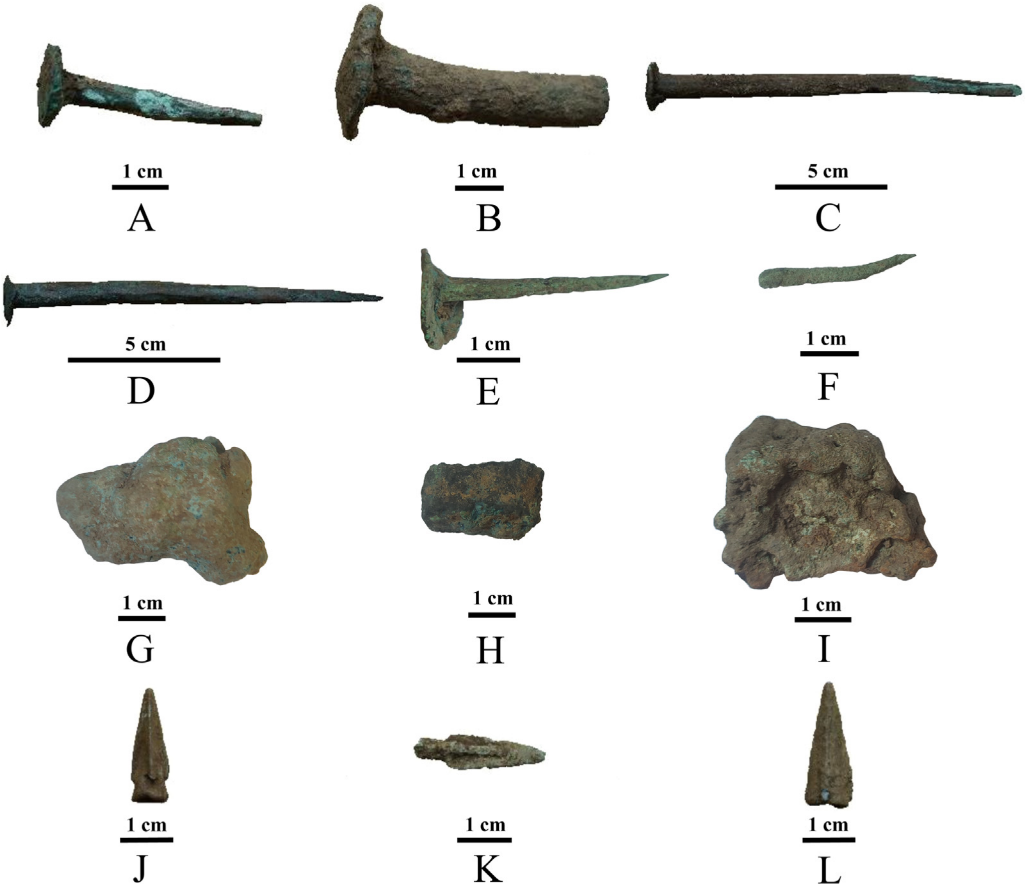

**Fig. 2.** Images of the analyzed finds from the archaeological site of Pyrgi. A-F: nails, G-I: *aes rude*, J-L: arrowheads.

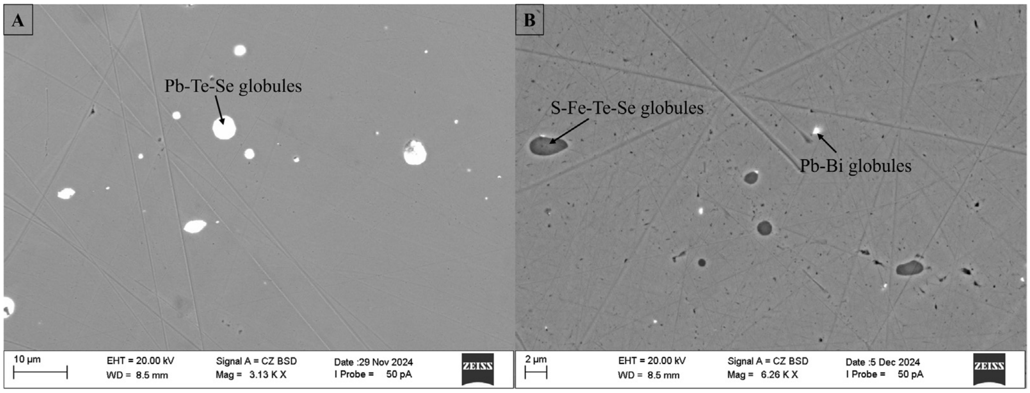

**Fig. 3.** BSE images of inclusions presented in the nails. (A) nail 9787, Pb-Te-Se globules in the copper matrix. (B) nail 58,257 globules of S-Fe-Te-Se and Pb-Bi in the copper matrix.

#### 4.1.2. *The* aes rude

The chemical composition of the three *aes rude* revealed pure copper in 99BA28 and 07AD4, while P18.1290.3 contained ∼ 2 % Sn (Table S.1, Supplementary Materials).

Find 99BA28 shows a deeply altered structure, with porosity visible in dark holes due to corrosion that affects even the central areas (Fig. 4AIII). The corrosion propagates along the grain boundaries, following the microstructure (Fig. 4AI) [31]. In the corroded zones (Fig. 4AII-III), copper chlorides are identified, as revealed by EDS analyses (Table S.1). Pb globules with As or Bi and Cu-S rich inclusions are present in the matrix. The formation of these globules occurred at the interface between the copper grains, which solidified first, resulting in a segregation process [32,33]. During solidification, the still-liquid phases were pushed toward the interstitial zones, where they tended to accumulate; Pb was the last element to solidify, being immiscible with Cu [33,34]. In this process, Pb incorporated Cu-S inclusions, which are concentrated at the intersection points between the grains, thus contributing to the formation of characteristic heterogeneous microstructures [32,35].

Sample 07AD4 showed a less altered internal structure than 99BA28, where low-iron copper sulfide inclusions and Pb-Bi-Ag globules were present. These inclusions, like those found in the first artifact, showed an intergranular distribution and the formation of the “eutectic intergrowth” between the matrix copper and the copper sulfide (Fig. 4BI-III) [36–38]. The microstructures were

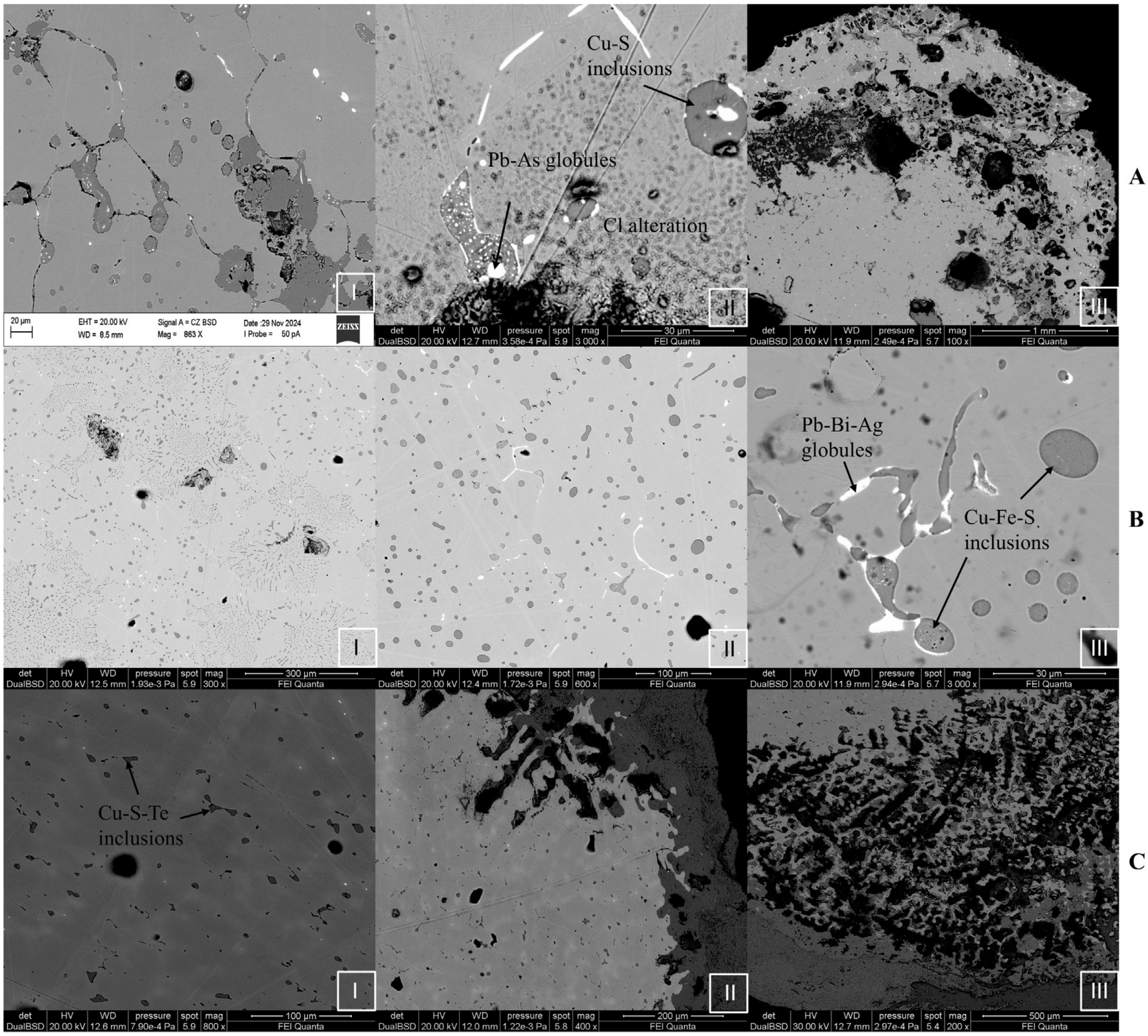

**Fig. 4.** SEM-BSE images of the three *aes rude* (99BA28, 07AD4, and P18.1290.3). (A) I-III: Finding 99BA28 shows Pb-As or Bi globules and Cu-S inclusions within the Cu matrix. (B) I-III: Finding 07AD4 shows Cu-Fe-S inclusions and intergranular distribution of Pb-Bi-Ag globules. Eutectic formations between copper and copper sulfide are visible in the images (B I). (C) I-III: Find P18.1290.3 shows a two-phase microstructure: one of pure copper (dark gray) and the second of copper and tin (light gray). The small Cu-S-Te and Pb globules solidify along the grain boundaries (C I-II). Corrosion, visible in (C III), follows the dendritic structure, with Sn depletion in the surface zone.

due to a low concentration of sulfides in the alloy, according to Schlegel and Schüller's Cu-S phase diagram [36].

Finally, sample P18.1290.3 had a different composition than the other two *aes rude*. SEM images showed the presence of a dendritic microstructure composed of two phases, *i.e.*, a Cu-rich (dark gray, 100 wt% Cu) and Cu-Sn-rich (light gray) phase. The latter has an average composition of 97.5 wt% Cu and 2.5 wt% Sn (Table S.1, Supplementary Materials). The Cu-S-Te inclusions and very small Pb-Bi-globules are dispersed in the second phase (Fig. 4CI) [10,21,23,39]. These inclusions are solidified along the grain boundaries (Fig. 4CI-II). The corrosion followed the trend of the dendrite arm structure (Fig. 4CIII), leading to the depletion of Sn in the most superficial zone and the formation of copper chlorides (Fig. S.4). In particular, EDS analysis carried out on the inclusions (Fig. S.4) showed that the presence of O (point 3) led to a decrease in the Cu and S contents relative to the inclusion without O (point 4); in both cases, however, Te remained largely unchanged (around 1.2 wt%). Furthermore, the mappings did not indicate that S-rich inclusions influenced the corrosion.

### 4.1.3. Arrowheads

All arrowheads are composed of three phases, *i.e.*, a copper phase (phase A), a copper-tin alloy (phase B), and lead islands (phase C) (Table S.1, Supplementary Materials). However, the distribution of these phases and their structural features differ significantly among the findings.

Sample 81.1098 shows an irregular distribution of the phases, with a concentration of the A phase in the inner portion, Pb near the outer portion, and the B phase throughout the sample. Fig. S.5 illustrates how the dendritic areas have a high Cu content (about 93.4 wt%; Table S.1), while a Sn-rich segregation phase (about 14.6 wt%; Table S.1) is present in the interdendritic areas, where Pb islands are also distributed. SEM maps highlighted the correlation between O and Pb.

Sample P18.1202.100 has a dendritic structure, with Pb islands and internal corrosion areas, where Cl and O concentrate (Fig. 5). Pb inclusions are present throughout the sample section but are more concentrated near the external corrosion layers (Fig. 6). A distinctive feature of this find was the selective enrichment that occurred in the outer zone, where Sn-enrichment is observed at the expense of Cu. Elemental maps also show a clear correlation between Cl and the distribution of Pb (Fig. 6).

Finally, sample 02BP48 has a heterogeneous internal structure, in which two zones with different morphologies can be distinguished. The east side has a regular dendritic structure, less pronounced in the core and more evident toward the outer portion.

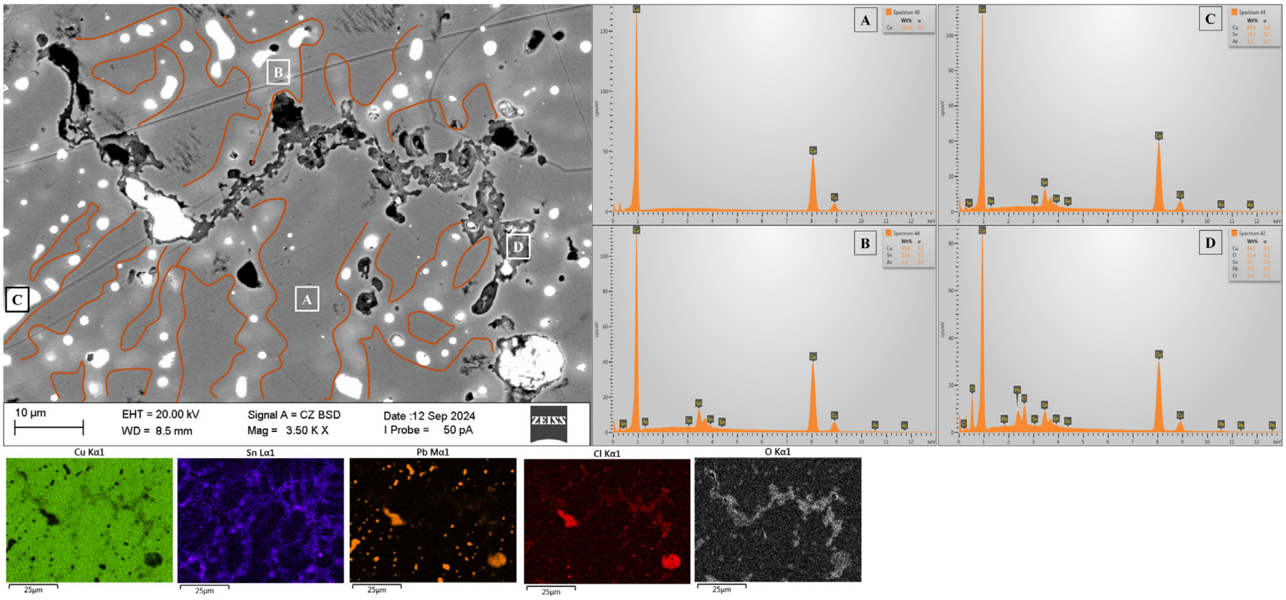

**Fig. 5.** SEM-BSD image and EDS analyses of the arrowhead P18.1202.100. The central image shows the microstructure of the sample, with dendritic regions (outlined in orange) and corrosion-affected areas. Four EDS spectra were acquired from the indicated points: (A) Cu-rich dendritic region; (B) Cu-Sn-As-rich interdendritic phase; (C) Pb inclusion; (D) corrosion zone enriched in O, Cl, and Pb. Elemental maps (Cu, Sn, Pb, Cl, O) are displayed at the bottom, illustrating the distribution of individual elements within the analyzed section and highlighting the association between Pb, O and Cl, particularly in the corroded regions.

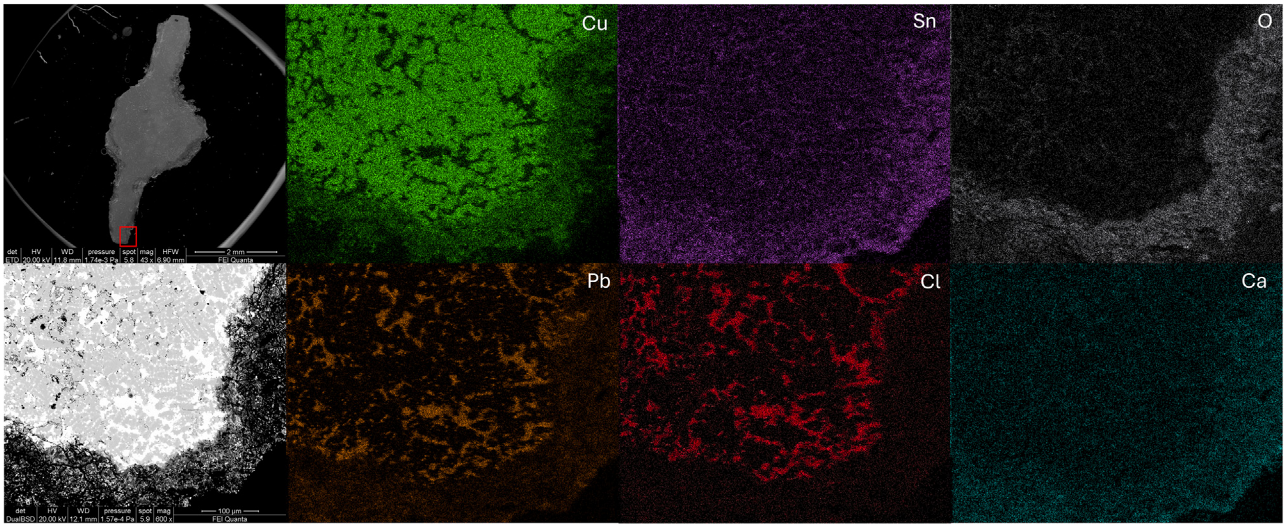

**Fig. 6.** EDS mappings of arrowhead P18.1202.100, in the outer area of the south fin, were obtained using the FEI-Quanta 400 tool. A phenomenon of surface enrichment of tin (Sn) is observed in the outer areas, indicative of a selective alteration process at the expense of copper (Cu).

The west side of the arrow is characterized by a branched structure composed of parallel dendritic arms (Fig. 7). Pb appears unevenly distributed within the sample, with a higher concentration in the fins than in the core. A general Pb-enrichment in the outer portions can also be seen, often related to the presence of Cl (Table S.1, Supplementary Materials).

### 4.2. Characterization of corrosion products and electrochemical properties

Micro-Raman spectroscopy was used to characterize the corrosion products detected in different areas of the artefacts (Table 2 and S.2). The predominant products are cuprite ($Cu_2O$) and malachite ($Cu_2CO_3(OH)_2$), common products of copper corrosion.

The corrosion layers of nails and *aes rude* were generally composed of copper oxides and carbonates. However, nail 9787 showed a multilayer corrosion structure due to the presence of atacamite $Cu_2Cl(OH)_3$, clinoatacamite $Cu_2Cl(OH)_3$, and nantokite CuCl in the outer part (Fig. 8). Two *aes rude* (samples P18.1290.3 and 99BA28) also revealed, in this case within the heavily corroded inner zones, the presence of atacamite (Fig. S.6). Instead, the arrowheads showed corrosion layers mainly consisting of copper oxides and carbonates, similarly to the other artifacts, although they were made of a more complex alloy rich in Sn and Pb. Only sample 81.1098 showed, in addition to corrosion products such as Cu oxides and carbonates present on the outer layer, intermediate layers containing cerussite ($PbCO_3$) (Fig. 9, spectrum E). The areas near the central cavity, probably created to insert the arrow shaft, are also investigated. Indeed, during the burial, this cavity gradually filled with sediment. Raman spectroscopy in this area highlighted the occurrence of cuprite and malachite (Fig. 9, spectra B and C), due to dissolution processes of the copper on the surface of the cavity.

Overall, the corrosion of the analyzed artefacts indicated two distinct ways: (1) the external layers composed of well-crystallized corrosion products as Cu oxides or carbonates, forming a "*passivat-*

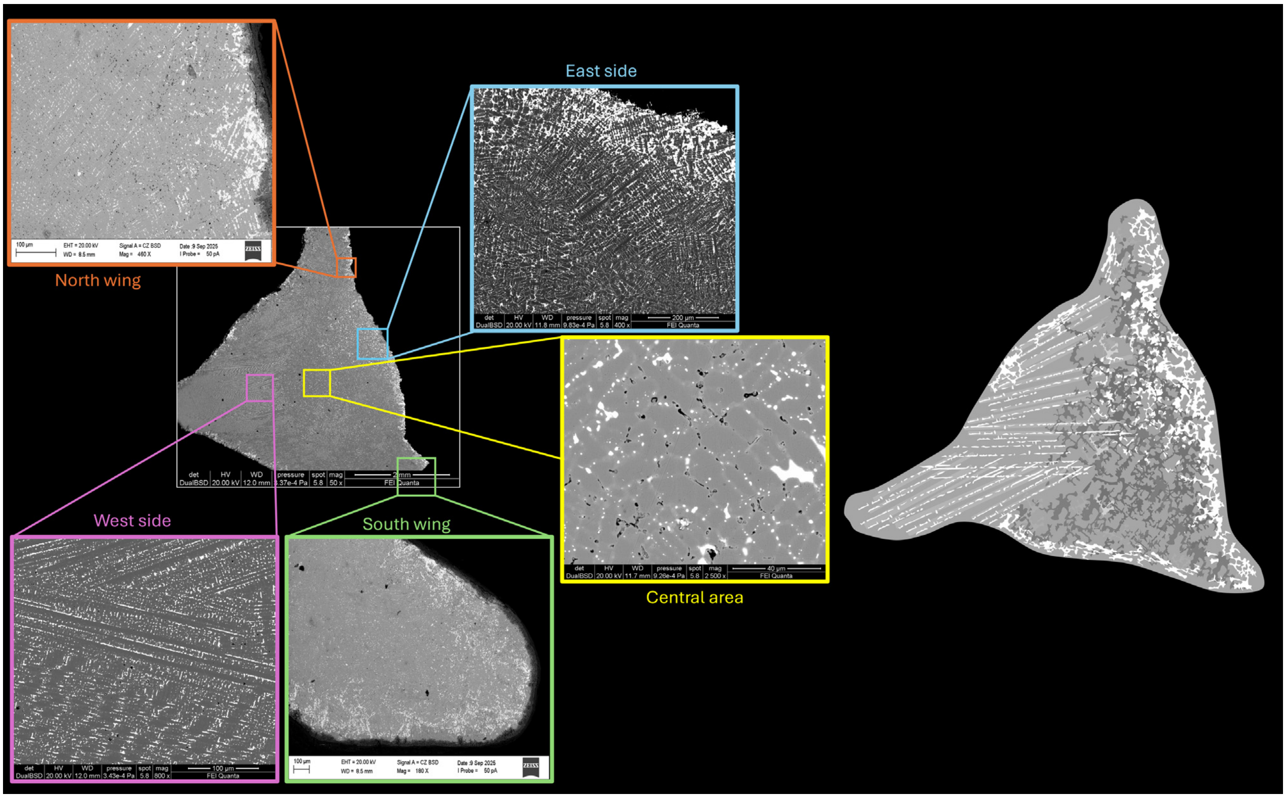

**Fig. 7.** SEM-BSE cross sections of sample 02BP48, highlighting microstructural changes in different areas of the arrowhead. Enlarged images show specific features of the north, south, east and west wings, as well as the central area. On the right, a stylized model depicts the entire arrowhead surface, with the characteristic structures reproduced graphically to indicate morphological differences between regions.

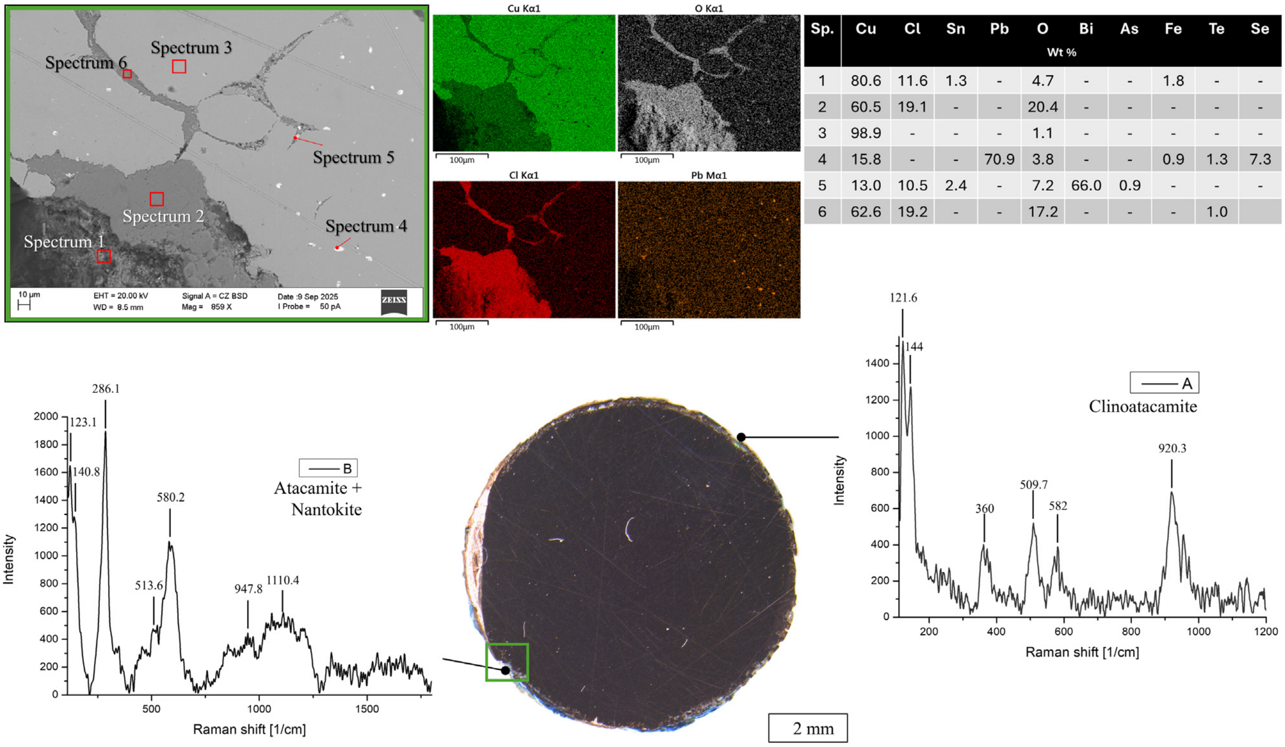

| Sp. | Cu | Cl | Sn | Pb | O | Bi | As | Fe | Te | Se |
|---|---|---|---|---|---|---|---|---|---|---|
| | Wt % | | | | | | | | | |
| 1 | 80.6 | 11.6 | 1.3 | - | 4.7 | - | - | 1.8 | - | - |
| 2 | 60.5 | 19.1 | - | - | 20.4 | - | - | - | - | - |
| 3 | 98.9 | - | - | - | 1.1 | - | - | - | - | - |
| 4 | 15.8 | - | - | 70.9 | 3.8 | - | - | 0.9 | 1.3 | 7.3 |
| 5 | 13.0 | 10.5 | 2.4 | - | 7.2 | 66.0 | 0.9 | - | - | - |
| 6 | 62.6 | 19.2 | - | - | 17.2 | - | - | - | 1.0 | |

**Fig. 8.** Cross section of nail 9787 at 30x magnification (Dino-Lite software). Raman analyses performed at the indicated points revealed the presence of chlorine-containing corrosion products: spectrum A shows the formation of clinoatacamite $Cu_2Cl(OH)_3$, while spectrum B reveals the coexistence of atacamite $Cu_2Cl(OH)_3$ and nantokite CuCl. The characteristic peaks used for the identification of the different compounds are listed in Table S.2. The green box highlights an 859x magnification of the selected area obtained with SEM, showing the EDS analysis points (spectra 1–6), whose results are summarized in the table on the right. Elemental maps display the distribution of Cu, O, Cl and Pb. The data confirm the presence of intermediate stages in the copper trihydroxychloride transformation sequence, which are responsible for the phenomenon known as “bronze disease.”.

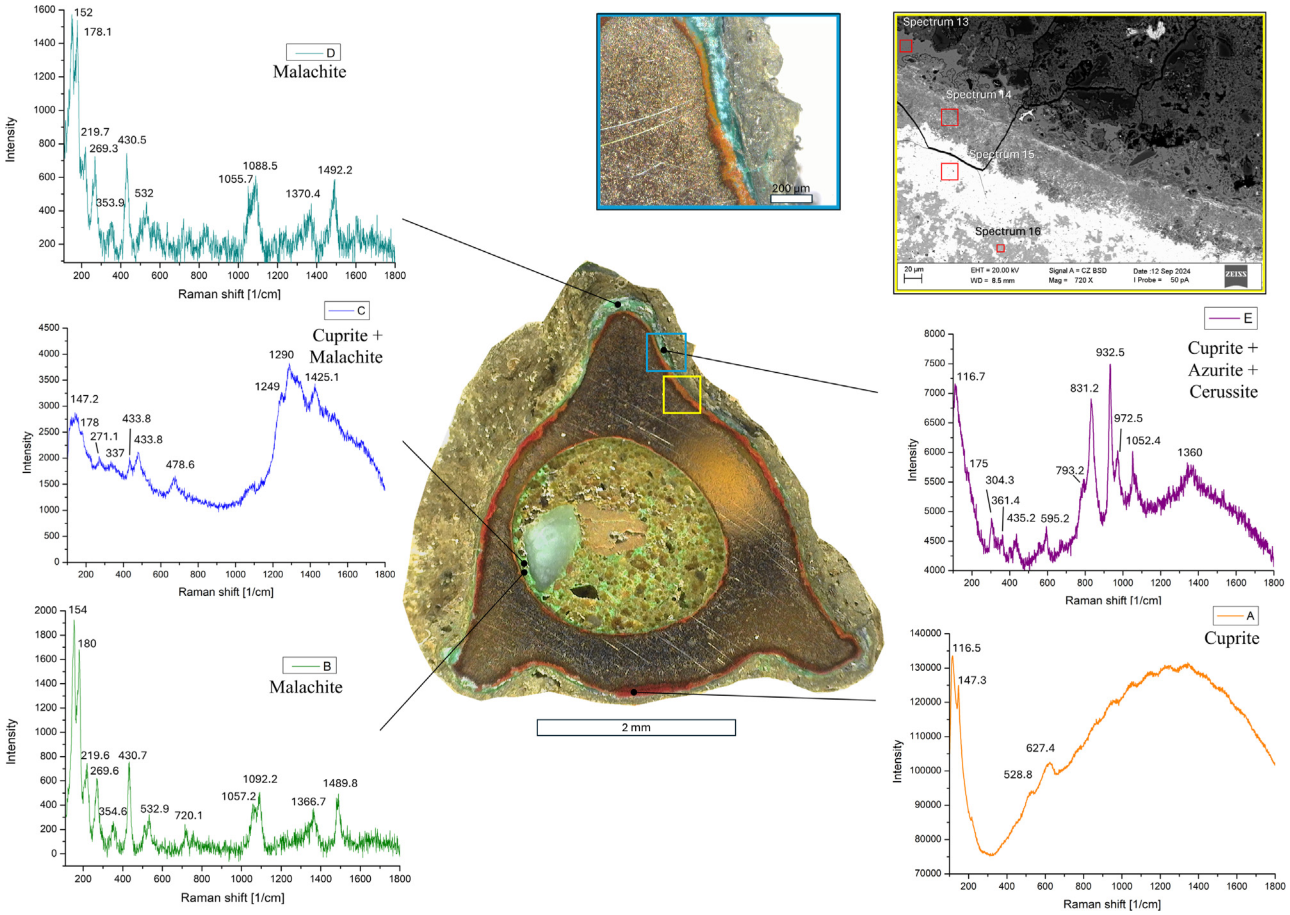

**Fig. 9.** Cross-section of the arrowhead 81.1098, at 30x magnification, acquired using the Dino-Lite handheld microscope. Points of Raman analysis have been highlighted in the image. Spectrum A shows the presence of cuprite ($Cu_2O$), while spectra B and D are attributed to malachite ($Cu_2CO_3(OH)_2$). Spectrum C reveals the coexistence of cuprite and malachite, while spectrum E identifies the presence of cuprite, azurite, and cerussite ($PbCO_3$). Table S.2 shows the identification peaks for each product. The blue box shows a 220x magnification of the area, highlighting the multilayer corrosion structure. The yellow box indicated an area analyzed by SEM-EDS; the corresponding spectra are reported in Supplementary Fig. S.7.

**Table 2**
Overview of corrosion products identified on each archaeological artifact.

| Inventory No. | Cpr[1] | Tnr[2] | Mlc[1] | Azr[1] | Cer[1] | Atc[3] | Cln[4] | Nnt[5] |
|---|---|---|---|---|---|---|---|---|
| 9787 | - | - | - | - | - | x | x | x |
| 58,257 | x | - | x | - | - | - | - | - |
| 49,466 | x | - | x | - | - | - | - | - |
| 52,640 | - | - | x | - | - | - | - | - |
| 04BG78 | x | - | - | - | - | - | - | - |
| 04BV57 | x | - | x | - | - | - | - | - |
| P18.1290.3 | x | x | - | - | - | x | - | - |
| 99BA28 | x | x | x | x | - | x | - | - |
| 07AD4 | x | - | x | - | - | - | - | - |
| 81.1098 | x | - | x | x | x | - | - | - |
| 02BP48 | x | x | - | - | - | - | - | - |
| P18.1202.100 | x | - | x | - | - | - | - | - |

**Cpr**: cuprite $Cu_2O$, **Tnr**: tenorite CuO, **Mlc**: malachite $Cu_2(CO_3)(OH)_2$; **Azr**: azurite $Cu_3(CO_3)_2(OH)_2$, **Cer**: cerussite $PbCO_3$, **Atc**: atacamite $Cu_2Cl(OH)_3$, **Cln**: clinoatacamite $Cu_2Cl(OH)_3$, **Nnt**: nantokite CuCl. The identification of corrosion products was carried out using both the Search-Match software of the instrument (Grams) and comparison with reference spectra taken from literature sources: [1][42], [2][43], [3][44], [4][45], [5][46]. Further information is provided in Table S.2 in the Supplementary Materials.

*ing layer*" [40,41]; while (2) the internal corrosion of the metallic core, which advances along intergranular paths or dendritic structures, sometimes showing the formation of copper chlorides. This internal degradation is often involved inclusions (*e.g.,* Pb), which were subject to selective corrosion and/or contribute to the local propagation of the corrosion front.

Fig. 10A shows the square wave voltammograms recorded on microparticulate deposits extracted from the corrosion layers of samples 04BV57, P18.12903, 58,257, and P18.1202.100, attached to graphite electrodes in contact with 0.25 M HAc/NaAc aqueous buffer solution at pH 4.75. In the first negative-going potential scan, a well-defined cathodic peak at ca. $-0.10$ V vs. Ag/AgCl is recorded. This signal corresponds to the overlapping reduction of cuprite, malachite, and eventually atacamite corrosion products to copper metal, while the corresponding reduction process of tenorite appears as a shoulder at ca. $-0.36$ V [29,30,47].

As already described in detail [29,47], the performance of successive potential scans leads to acquire information on progressively deeper regions of the corrosion layers based on the measurement of currents for the main reduction process, $i_1(\mathrm{N})$, and the tenorite reduction shoulder, $i_2(\mathrm{N})$ ($N$ being the scan number) [48,49]. Using the criterion for current measurement schematized in Fig. 10A(d), the values of the above currents and the accumulated currents, $I_J(N)$ $(= i_J(1) + i_J(2) + \ldots\ i_J(\mathrm{N});\ J = 1{,}2)$ can be determined. The accumulated quantities can be taken as representative of the net charge transfer passed during the respective reduction process, which in turn represents the depth of the corrosion pattern of the object. Since the sampling process does not transfer the same quantity of sample onto the electrode surface, the absolute values of currents and accumulated currents can vary between individual experiments. However, they define common patterns that can be able to group the samples studied. Fig. 10B shows the plot of the $I_2(6)/I_1(6)$ ratio vs. $I_1(6)$ for samples in this study. One can

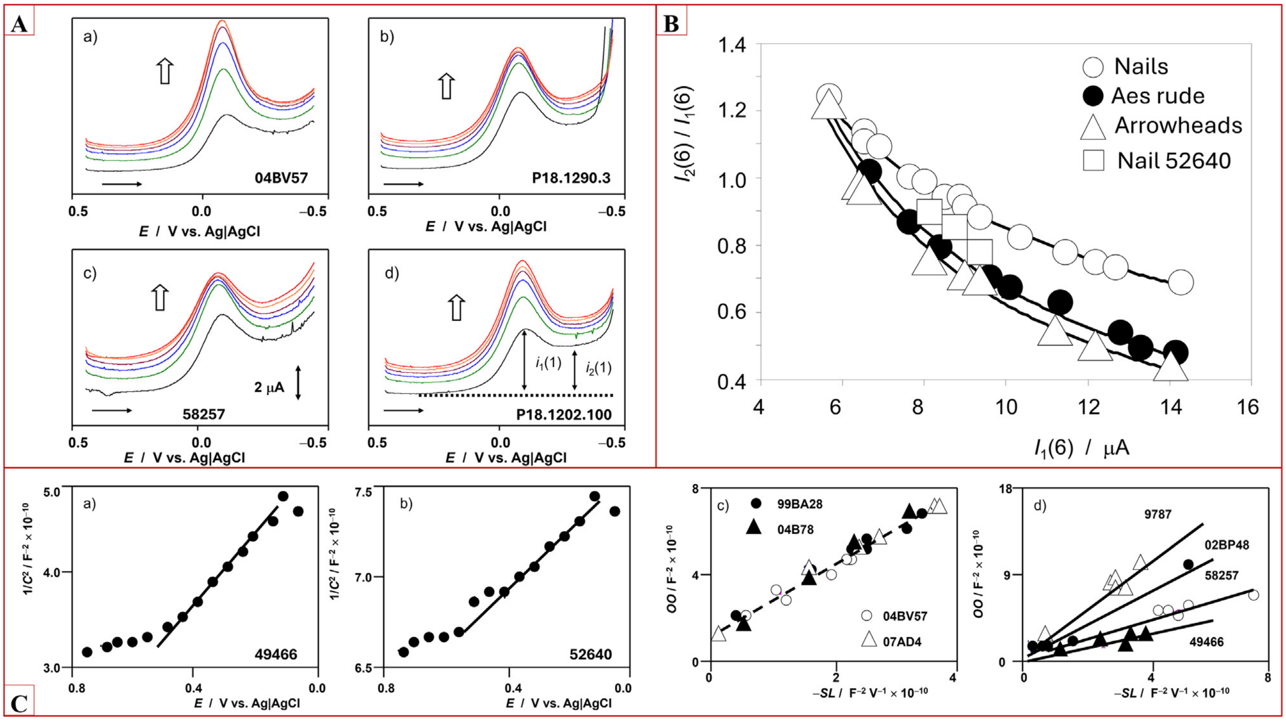

**Fig. 10.** Electrochemical analysis. (A) Square wave voltammetry of samples a) 04BV57, b) P18.12903, c) 58,257, and d) P18.1202.100, attached to graphite electrodes in contact with 0.25 M HAc/NaAc aqueous buffer solution at pH 4.75. Potential scan initiated at 0.45 V in the negative direction; potential step increment 4 mV; square wave amplitude 25 mV; frequency 10 Hz. Six successive potential scans are superimposed, whose order is denoted by vertical arrows. The horizontal arrows mark the direction of the potential scan. The baseline and the criterion used to measure currents are depicted in (d) for the first potential scan. (B) Plots of $I_2(6)/I_1(6)$ vs. $I_1(6)$ for nails (circles), *aes rude* (solid circles), and arrowheads (triangles) in this study using voltammetric data such as illustrated in Fig. 10A. Three independent measurements for each object are plotted. The data point for nail 52,640 is represented by squares. The solid lines correspond to the fit of experimental data to potential functions. (C) a,b) Mott-Schottky plots obtained from impedance data of samples a) 49,466 and b) 52,640. c,d) Plots of the ordinate at the origin vs, the (minus) slope for samples from the Southern Sanctuary (c) and the Monumental Sanctuary (d).

see in this figure that the data points for the *aes rude* and arrowheads can be fitted to two closely similar curves, representative of slightly different corrosion patterns. Except for nail 52,640, data points for nails differ from the above and define a different curved trend.

Fig. 10C (a,b) shows the Mott-Schottky (MS) plots of $1/C^2$ ($C$, capacitance, F) values vs. applied potential ($E$, V vs. Ag/AgCl) from impedance measurements in the region of potentials between 0.0 and +0.8 V vs. Ag/AgCl, where no faradaic processes occur. The recorded data at sample-modified electrodes produces MS plots with reasonable linearity. The slope of such representations is negative, in agreement with the *p*-type semiconducting character of cuprite, which is, in principle, the main corrosion product in the sampled regions of the artifacts. The slope and the ordinate at the origin of these representations (or, equivalently, the abscissa at the origin, in turn representative of the flatband potential of the semiconducting material) calculated in independent replicate impedance measurements vary because of the different net amount of sample transferred onto the electrode in each measurement. However, the representations of the intercept vs. the (minus) slope yield straight lines, as expected if the MS model applies [30]. Fig. 10C (c,d) shows the representations corresponding to samples from the Southern Sanctuary and the Monumental Sanctuary of Pyrgi.

Samples from the Southern Sanctuary display quite a homogeneous response (Fig. 10C). Similar homogeneity was obtained for samples from the Public Ceremonial quarter. In contrast, the samples from the Monumental Sanctuary present different trends. To interpret these features, it is convenient to remark that the sampling process results in the transference of a series of metallic sheets of nanometric size onto the graphite electrode surface [29,30,47]. In repetitive voltammetry, there is a progressive delamination of the metallic sheets, and the properties of deeper regions of the corrosion layers influence the electrochemical response. In MS measurements, however, no electrolysis takes place, and the technique provides information on the more external region of the corrosion layers. Since this region is more sensitive to the environment, its capacitance behavior mainly reflects not the composition and microstructural properties of the more external corrosion layers, in turn is quite sensitive to the environmental conditions.

## 5. Discussion

Among the samples, differences in chemical composition of the alloys and inclusions, microstructure, and corrosion have been observed. The nails and *aes rude* are almost pure copper with very low percentages of tin and lead. Only two finds (49,466 and P18.1290.3) contain about 2 wt% of Sn. The arrowheads are made by a ternary bronze alloy (Cu-Sn-Pb), with tin between 2 and 8 wt% (low-tin bronze) and a high Pb content, between 3 and 21 wt% (Table S.1, Supplementary Materials). These results indicated the skill of ancient Etruscan metallurgists in adapting the properties of alloy to functional needs.

Lead, often present in copper-based alloys, originated either from naturally occurring impurities in the ores or was intentionally added to lower the melting point and improve castability [33]. In arrowheads, Pb abundance suggests a deliberate choice to increase weight and improve the ability to penetrate upon impact on the target [50]. Arrowheads with high Pb content have been found in various archaeological contexts and associated with different ancient civilizations [6,50–53].

On a micrometer scale, the arrowheads show a dendritic structure (Fig. 5, 7, and S.5), indicative of a production process by casting with rapid cooling. [33]. In Cu-Sn-Pb alloys, Cu solidifies as the first component ($T_f$°: 1084 °C), forming the skeleton of the dendritic structure, where the less soluble elements are concentrated inside [33]. Lead does not participate in the formation of a copper-tin alloy, being insoluble with copper, but creates segregated islands between the interdendritic spaces [54–56]. In this case, the high concentration of Pb makes the alloy too brittle for cold working, explaining the absence of signs of subsequent processing [57].

Arrow 02BP48 shows signs of faster cooling than the other finds, with a dendritic structure extending to the core, despite its lower tin percentage (about 2 wt%). The west wing shows a more regular dendritic structure, with the B and C phases aligned parallel (Fig. 7) and a higher concentration of Pb islands. This was also evidenced by the average composition obtained from X-ray mappings, where the Pb is enriched up to 9.4 wt%, compared to the 3 wt% value found in the central area (Table S.1, Supplementary Materials). This phenomenon could have been attributed to the position of the mold during casting. The effect of gravity may have favored the accumulation of Pb, a denser element, in one of the fins.

Arrowhead 81.1098 has a central cavity, filled by minerals from the burial soil, which affect the internal structure of the artifact. The variation in thickness between the outer surface and the surface bordering the cavity in the inner area resulted in differences in the cooling rate, *i.e.*, thinner parts cooled faster than thicker parts. This variation caused a different effect on the distribution of Pb in the alloy. In areas with a faster cooling rate, Pb tended to be enriched in the outermost and central areas (Fig. S.8). This could have been due to two phenomena, *i.e.,* the first is the "reverse surface segregation," formed when solidification began rapidly, such as near a mold wall. In this case, Pb-concentration on the surface was due to the shrinkage of solidification and the need to compensate for shrinkage, causing the surface composition to be richer than inside. The second, "positive segregation", occurred in the inner regions of the object and results from the inward thrust of denser components, such as lead, during the formation of dendritic phases [58,59].

Nails and *aes rude* differ in composition, being predominantly pure copper with minimal amounts of Sn and Pb (Table S.1), excepting nail 49,466 (2.2 wt% Sn) and *aes rude* P18.1290.3 (2.5 wt% Sn). These show two-phase structures with regions rich in Cu (phase A, dark gray) and others in Cu-Sn (phase B, light gray), as well as Pb-Te, Cu-S-Te, and Pb-Bi inclusions (Figs. S.2 and 4). Their presence suggests the use of polymetallic sulfides as raw materials for extraction, such as chalcopyrite or stannite [60].

Tellurium and selenium have been found in several artefacts, associated with copper sulfide and lead inclusions. Indeed, tellurium and selenium were often related to ores of copper, lead, gold, and other heavy metals [15,61]. Both elements were enriched in sulfide minerals through hydrothermal processes, particularly in volcanogenic massive sulfide deposits (VMS). Selenium replaces sulfur, due to their chemical affinity and similarity of ionic radii, in the crystal structures of minerals such as pyrite, galena, sphalerite, and chalcopyrite [16]. This isomorphic substitution is a common phenomenon in various metallurgical and geologic systems and can affect the final composition of sulfidic inclusions, leading to variations in Se content from the original sulfur [62,63]. Instead, tellurium tends to preferentially concentrate in ores containing noble metals, *i.e.*, Ag and Au, and in Pb and Cu sulfides [16,17].

Previous studies reported that Te and Se tended to become trapped in sulfide inclusions when the smelting process did not remove all sulfur; thus, both elements could have occurred in low concentrations in the final products [10,17,21,64,65]. In hydrothermal systems, for example, VMS deposits, Se and Te behave as chalcophile elements, preferentially binding to metal ions rather than remaining in solution. The incorporation of Se and Te into minerals is aided by temperature between 250 and 350 °C, where sulfide precipitation occurred due to the cooling of hydrothermal fluids flowing through volcanic and sedimentary rocks [16].

In VMS deposits, Se could have been released from pyrite and chalcopyrite during hydrothermal leaching or supergene alteration processes, contributing to its mobilization and redistribution in secondary mineralogical phases. Tellurium, being less mobile than Se, tends to be trapped in primary minerals or to form separate tellurides in associated metal ores [16].

The low presence of Te and Se in artifacts is also related to their volatility, since copper sulfides must be oxidized ("roasting") to remove sulfur before they can be reduced [21,66]. The process occurs at temperatures around 700 °C, involving the partial loss of Te and Se, and varying the concentrations [64]. Although this behavior may have influenced the absolute concentrations of Te and Se, they are good indicators for understanding production technologies, the degree of oxidation, and roasting temperatures, and provide clues to the ores [64]. These elements reflect both the geochemical composition of the ore source and the incomplete smelting process, which did not allow their complete removal. EDS analyses showed Te and Se exceeding 4 wt% (Table S.1), indicating the nails originated from similar deposits, perhaps from subduction zones such as those in MVS systems; an example in the ancient Mediterranean areas was the deposits of Cyprus. Selenium is preferentially incorporated into pyrite and chalcopyrite, while Te is associated with galena and other lead and silver ores [16,67].

The presence of Te, Se, and Bi in the inclusions of the artifacts also found parallels in several hydrothermal polymetallic deposits of the Italian peninsula, such as southern Sardinia, the Western Alps, and Liguria [68]. In the Arburese district (southwestern Sardinia), *e.g.*, Se was found enriched up to 4 wt% in galena or sulfur-rich carbonaceous black shales of Silurian age. Instead, the Piazza deposit in Liguria was characterized by a Te-rich mineralogy (*e.g.,* native Te phases and PbSe containing Te), in association with Ag–Pb–Cu sulfides [68].

In a recent study [14], it was reported that the transport of nano-micron metal-rich sulfide-sulfosalt melts within epithermal fluids (at temperature <400 °C) formed irregular and bleb-like poly-mineral inclusions of Ag-Au-Cu-Pb(-Fe-Zn)-As-Sb-S-Se upon cooling. These hydrothermal systems demonstrated that metals such as gold and silver could be transported not only as soluble complexes, but also as transient, non-soluble molten droplets suspended in hydrothermal fluids [14]. These droplets often carried associated chalcophile and semi-volatile elements, including Bi, Te, and Se, which may crystallize together upon cooling. The morphology and elemental composition of some inclusions observed in the Pyrgi artifacts—such as Pb-Te-Se or Pb-Bi globules—could thus have reflected solidified micro-droplets inherited from polymetallic sulfide ores formed in hydrothermal environments.

One of the questions raised by archaeologists concerned the possibility that the *aes rude* was remelted to produce nails. In literature, the *aes rude* was described as rough, shapeless masses of metal [2,69,70], with high compositional variability in the alloys and inclusions, due to ore deposits and the metallurgical practices. Commonly, *aes rude* was composed mainly of Cu with inclusions of S-Fe and Pb [2,69]. The absence of tin and the high iron content indicated that this *aes rude* was unsuitable for plastic deformation or forging, suggesting production aimed at maximizing metal yield rather than the quality of the finished product [2]. This reinforced its possible symbolic or votive value, where the abundance of metal was more important than its metallurgical quality. Studies on other *aes rude* from Pyrgi revealed a chemical composition similar to that of the studied samples, consisting of a Cu matrix with large inclusions of Fe oxides, globules of Cu-Fe sulfides, and inclusions rich in Bi (66 %), Cu (22 %), and Pb (4 %) [70].

In the skarn deposits of Campiglia Marittima (Tuscany, Italy) [39,71] and in the Usseglio district (Western Alps) [68], copper-bearing polymetallic ores with Bi-rich sulfide phases are known to be present [72]. Lead globules of sample 07AD4 also contained Ag and Bi [73]. Silver was often bound from Pb ores, as its presence was commonly associated with Cu-Pb-Zn sulfides in polymetallic ore deposits [39], such as those from Tuscany [71] and Sardinia [74].

The *aes rude* studied in this work do not contain inclusions of Te and Se, which is consistent with the results of a previous study of other *aes rude* also from Pyrgi [70]. This data does not support the hypothesis of the reuse of *aes rude* to create other artifacts, such as nails. Only P.181290.3 shows Te, about 1 wt%, localized in S-Cu inclusions. However, observation of the sample (Fig. 2H) reveals a more regular shape, which differs from the typical rough and irregular morphology of *aes rude*, suggesting that this find does not belong to this type of artifact, but instead may be a fragment of another object.

Nail 49.466 shows “banded” phases in the outer layers, suggesting cold working after casting [33,75,76]. This, together with the addition of Sn, could indicate an alternative use of the nail to others [13,33,77]. Nail 04BV57 was not sampled but shows a surface composition consistent with the other copper nails.

Copper is a softer metal than bronze or iron, and it would seem less suitable for objects that must be subjected to structural stress, as nails usually are. The most plausible hypothesis is that nails, especially the larger ones, were used to fix terracotta decorations to the wooden structures of the temple [9,78]. However, copper nails found in shipwrecks [79–83] or in port contexts [82] are documented in the literature, suggesting a possible use in ship carpentry. Pyrgi was a commercial crossroads because of its port. Thus, the nails could have represented tools used in the naval sector; however, the context of the find, near sanctuaries, favored the interpretation related to the use of these tools in sacred architecture [9,78].

Micro-Raman analyses performed on the cut sections of the finds revealed a layered corrosion structure, which consisted of an inner layer of cuprite ($Cu_2O$), overlaid by an external layer of malachite ($Cu_2CO_3(OH)_2$). The presence of cuprite and malachite indicates the formation of a passivating patina that protects the artifact’s surface from further degradation [40]. Active corrosion phenomena were exclusively observed in nail 9787 and in two *aes rude* (P18.1290.3 and 99BA28), where localized zones of aggressive alteration were identified. These were associated with the presence of hydroxychlorides, including atacamite for all three samples, and clinoatacamite, and nantokite only in nail 9787 (Figs. 8 and S.6). Although atacamite and clinoatacamite are polymorphs ($Cu_2Cl(OH)_3$), they can be distinguished by their crystallographic features and exhibit slightly different levels of chemical stability [84,85]. Both compounds may result from the transformation of less stable copper hydroxychlorides, such as botallackite, under varying environmental conditions [77,86]. Their occurrence in samples suggests a relatively recent corrosion process. Instead, the detection of nantokite (CuCl) in the innermost layers of the patina indicated a still active corrosion, as this compound is the first step in the copper chloride transformation process [87]. Nantokite is unstable in the presence of moisture and oxygen, and it tends to react rapidly, starting a self-catalytic cycle of degradation. Consequently, its presence indicated that corrosion was progressing, irreversibly leading to the “bronze disease” phenomenon [77,84,87,88]. In sample 9787, the alteration occurred only in a few areas, circumscribed within a generally compact and well-structured corrosion layers, suggesting a pitting phenomenon. Lead inclusions in the nail may have facilitated this process. During solidification, lead, which does not form an alloy with copper and solidifies later, tends to segregate at the grain boundaries as globules. Therefore, since Pb is less noble than copper, it is subject to selective corrosion, leading to its dissolution and opening preferential pathways for deeper penetration of corrosion (Fig. 8) [76,89]. The occurrence of nantokite and localized corrosion along grain boundaries, where Pb inclusions are present, may have triggered self-powered corrosion processes, leading to the progressive degradation of the alloy, compromising its structure [77,90]. Instead, the investigations carried out on the inner areas of the *aes rude* confirmed the results previously obtained with SEM, which had revealed an association of Cl and Cu in the corroded zones, later substantiated by the identification of atacamite (Figs. S.4 and S.6).

Although other artifacts were recovered from the same archaeological area (Table 1), Raman spectroscopy did not reveal the presence of chloride-based corrosion products. This suggested that the samples containing copper hydroxychlorides may have been exposed to more aggressive environmental conditions. Pyrgi is, in fact, a coastal archaeological site facing the Tyrrhenian Sea, and as discussed in the geological context section (Section S.2 in the Supplementary Materials), previous studies on the soil of the Monumental Sanctuary and the two temples indicate the possible accumulation of brackish water in the subsoil [91]. It is therefore plausible that some artifacts were buried in a microenvironment locally affected by saline infiltration. These conditions may have played a key role in promoting the formation of copper hydroxychlorides.

Sample 81.1098 shows multilayer corrosion (Fig. 9) consisting of (1) a green layer of malachite (spectrum D), more concentrated in the fins, (2) a homogeneous red layer of cuprite surrounding the entire artifact (spectrum A), and (3) an intermediate layer with the presence of cuprite, azurite, and cerussite (spectrum E). Cuprite is a protective barrier that limits corrosion penetration and preserves the original surface. In the inner area of the sample, a cavity filled with soil was observed. In this area, stratified alteration products were identified, likely resulting from the interaction between the metallic substrate and the exogenous mineral particles. This contact appears to have promoted the localized formation of secondary corrosion phases, such as copper oxides and carbonates (Spectra B and C).

The external corrosion layers of arrowhead P18.1202.100 shows a Cu decrease and an Sn increase (Fig. 6). This type of selective depletion is referred to as decuprification [41,92,93]. This is due to prolonged exposure to soil conditions that promote the preferential dissolution of Cu [41,94,95]. The presence of Sn-enriched corrosion products (such as oxides) limits the diffusion of further degradation processes by forming a passivating barrier [41,96–98]. This occurs because they have lower conductivity, reducing the internal transport of $O_2$ and/or aggressive species (*e.g.*, $Cl^-$) and, at the same time, hindering the release of $Cu^+/Cu^{2+}$ to the outside, slowing down corrosion [96,99,100]. Despite the observed tin enrichment, Raman spectroscopy did not detect peaks attributable to Sn-based crystalline phases, due to their low crystallinity, weak Raman scattering power, or amorphous nature within the corrosion matrix of this sample [98]. Furthermore, the presence of other corrosion products with stronger Raman scattering, such as cuprite, may have overlapped and masked any signals associated with Sn oxides [98].

In the corroded areas of all arrowheads with high lead content, a clear correlation was observed between Pb inclusions and the presence of Cl (SEM maps, Figs. 5 and 6). This suggests the activation of galvanic microcells in humid conditions, which facilitate deeper penetration of corrosive agents [101]. In contrast, in Cu-artifacts the corrosion tended to develop diffusely along the grain boundaries. S-Fe-Te-Se-based inclusions did not appear to significantly influence corrosion (Fig. S.4).

VIMP results were consistent with previous analytical data, revealing the different nodular structure and composition of the different groups of objects (Fig. 10B). As previously described, the “anomalous” nail 52,640 differed from the other by the presence of globular inclusions rich exclusively in sulfur and iron. This sample also shows voltammetric behavior differing from the other nails. As can be seen in Fig. 9B, the $I_2(6)/I_1(6)$ values of nail 52,640 fall in a tendency curve below that defined by all other nails. Since the $I_2(6)/I_1(6)$ ratio can be considered as representative of the averaged tenorite/cuprite ratio in the sampled corrosion layer [48,49], these features can tentatively be attributed to the occurrence for sample 52,640 of corrosion in a quite different, less oxidant environment.

MS data in Fig. 10C indicate that samples from the Southern Sanctuary (consisting of nails and *aes rude*) and the Public Ceremonial quarter (*aes rude* and arrowheads) showed quite homogeneous impedance behavior regardless of the type of artifact, thus suggesting relatively uniform conditions of corrosion. This was a sharp contrast with the samples from the Monumental Sanctuary (nails exclusively), which showed quite different MS plots. This could be rationalized by considering that, apart from possible differences in composition and microstructural properties of the base metal, the nails were possibly subjected to more severe conditions, likely due to the presence of brackish water in the subsurface. In line with this explanatory scheme, the sample 9787, where atacamite and nantokite (markers of advanced corrosion) were detected, showed the highest deviation relative to the MS response of all other nail samples.

## 6. Conclusions

The results on nails, arrowheads, and *aes rude* indicated chemical and microstructural differences among artifacts, reflecting the ability of artisans to select different alloys for functional and cultural reasons. The study also provided insights into the raw materials and metallurgical practices, and the state of preservation of the artifacts.

1. The nails and the *aes rude* consisted of inclusions-rich pure copper, while the arrowheads were in a Cu-Sn-Pb alloy with a high lead content, characterized by patterns of dendritic solidification and Pb segregation.
2. The inclusions in the *aes rude* suggest that the artisans adopted an approach focused more on maximizing metal recovery than on refining the quality of the final product. Fe, S, Te, and Se inclusions suggest the use of polymetallic sulfide ores, probably from Italy and Cyprus VMS deposits. Bi-rich phases in Pb inclusions infer hypotheses that the raw material originates from Tuscan deposits, Campiglia Marittima, or the Western Alps, Usseglio district. Te and Se give information about refining and technological knowledge.
3. Cuprite and malachite indicate relatively stable corrosion products, while trihydroxychlorides were detected in samples 9787, P18.1290.3, and 99BA28, highlighting severe corrosion processes and exposure to chloride-rich environments. Electrochemical investigations revealed variations in corrosion behavior among the artifacts recovered from different areas of the site. In particular, the nails found in the Monumental Sanctuary showed more pronounced anomalies in the Mott-Schottky analysis results, suggesting greater variability in corrosion processes than in the other contexts, likely due to the presence of seawater infiltration.

## Funding

Sapienza University of Rome (Grant of 2021 and PhD mobility award funds) is gratefully acknowledged, as well as financial support from Project PID2020-113022 GB-I00 supported by MCIN/AEI/10.13039/501100011033, Fondo Europeo de Desarrollo Regional (ERDF), and Agencia Estatal de Investigación (AEI), and Project AICO/2021/095, which is supported with Generalitat Valenciana and Fondo Europeo de Desarrollo Regional (ERDF).

## Supplementary materials

Supplementary material associated with this article can be found in the online version at doi:10.1016/j.culher.2025.10.021.

## References

[1] L.M. Michetti, Cerveteri e Pyrgi, il porto, “Gemello” sul Tirreno, in: P. Desantis, E. Govi, V. Nizzo, G. Sassatelli, T. Trocchi (Eds.), Spina Etrusca. Un grande Porto Nel Mediterraneo, Catalogo Della Mostra (Ferrara 2022-2023), ARA Edizioni, Roma, 2023, pp. 209–222.

[2] G.M. Ingo, T. de Caro, G. Bultrini, Microchemical investigation of archaeological copper based artefacts disclosing an ancient witness of the transition from the value of the substance to the value of the appearance, Microchim. Acta 144 (2004) 87–95, doi:10.1007/s00604-003-0097-y.

[3] G. Saviano, F. Felli, M. Cavallini, L. Drago, Study of an Etruscan object composed of three metals, Period. Mineral. 71 (2002) 217–225.

[4] M. Abdelbar, A.Roshdy Elsakhry, Archaeometallurgical characterization of Greco-Roman copper-based and iron nails from Tel Abu Seify, North Sinai, Egypt, J. Archaeol. Sci. Rep. 59 (2024) 104815, doi:10.1016/j.jasrep.2024.104815.

[5] M. Bernabale, F. Cognigni, F. Mura, L. Nigro, D. Montanari, M. Rossi, C. De Vito, 3D imaging of micro-segregation and corrosion behavior of alloying elements in archaeological artefacts from Motya (Sicily, Italy), Corros. Sci. 211 (2023) 110900, doi:10.1016/j.corsci.2022.110900.

[6] M. Bernabale, L. Nigro, D. Montanari, C. De Vito, Exploring the chemical composition and corrosion patterns of arrowheads used in the Siege of Motya (397 BC) through a multi-analytical approach, J. Cult. Herit. 52 (2021) 146–152, doi:10.1016/j.culher.2021.10.001.

[7] R.J. Mercer, Metal arrow-heads in the European bronze and early iron ages, Proc. Prehist. Soc. 36 (1970) 171–213, doi:10.1017/s0079497x0001313x.

[8] J. Baron, J. Puziewicz, K. Nowak, D. Sych, B. Miazga, M. Ziobro, Same but different. Composition, production and use of bronze arrowheads from the Late Bronze Age deposit from Wrocław-Widawa in SW Poland, J. Archaeol. Sci. Rep. 32 (2020) 1–18, doi:10.1016/j.jasrep.2020.102459.

[9] L.M. Michetti, A. Conti, I metalli a Pyrgi tra circolazione, tesaurizzazione e offerta, in: M.C. Biella, C. Carlucci, L.M. Michetti (Eds.), Produrre Per Gli dèi. L’economia Per Il Sacro Nell’italia Preromana (VII-II sec. a.C.), Edizioni Quasar, Roma, 2022, pp. 269–301.

[10] D. Hook, The composition and technology of selected Bronze Age and early Iron Age copper alloy artefacts from Italy, prehistoric Metal artefacts from Italy (3500-720 BC) in the British Museum, British Museum Research Publication 159 (2007) 308–351.

[11] P. Valério, R.J.C. Silva, M.F. Araújo, A.M.M. Soares, F.M.B. Fernandes, Microstructural signatures of bronze archaeological artifacts from the Southwestern Iberian Peninsula, MSF 636–637 (2010) 597–604, doi:10.4028/www.scientific.netMSF.636-637.597.

[12] E. Figueiredo, P. Valério, M.F. Araújo, R.J.C. Silva, A.M. Monge Soares, Inclusions and metal composition of ancient copper-based artefacts: a diachronic view by micro-EDXRF and SEM-EDS, XRS 40 (2011) 325–332, doi:10.1002/xrs.1343.

[13] G.M. Ingo, T. de Caro, C. Riccucci, E. Angelini, S. Grassini, S. Balbi, P. Bernardini, D. Salvi, L. Bousselmi, A. Çilingiroglu, M. Gener, V.K. Gouda, O. Al Jarrah, S. Khosroff, Z. Mahdjoub, Z. Al Saad, W. El-Saddik, P. Vassiliou, Large scale investigation of chemical composition, structure and corrosion mechanism of bronze archeological artefacts from Mediterranean basin, Appl. Phys. A 83 (2006) 513–520, doi:10.1007/s00339-006-3550-z.

[14] N. Cano, J.M. González-Jiménez, A. Camprubí, E. Morales-Casique, E. González-Partida, Transient non-soluble noble metal transport in hydrothermal ore systems, Nat. Commun. 16 (2025) 1–9, doi:10.1038/s41467-025-57740-7.

[15] M. Filella, C. Reimann, M. Biver, I. Rodushkin, K. Rodushkina, Tellurium in the environment: current knowledge and identification of gaps, J. Environ. Chem. 16 (2019) 215–228, doi:10.1071/EN18229.

[16] W. Zhang, F. Zhang, Y. Wang, J. Wang, J. Liu, H. Zhang, Q. Shi, W. Gu, K. Wang, X. Du, A review of geological characteristics and selenium enrichment in Se-bearing volcanogenic massive sulfide deposits, Int. Geol. Rev. 67 (2024) 1306–1321, doi:10.1080/00206814.2024.2434873.

[17] F.M. Makuei, G. Senanayake, Extraction of tellurium from lead and copper bearing feed materials and interim metallurgical products – a short review, Miner. Eng. 115 (2018) 79–87, doi:10.1016/j.mineng.2017.10.013.

[18] L. Roca-Perez, C. Gil, M.L. Cervera, A. Gonzálvez, J. Ramos-Miras, V. Pons, J. Bech, R. Boluda, Selenium and heavy metals content in some Mediterranean soils, J. Geochem. Explor. 107 (2010) 110–116, doi:10.1016/j.gexplo.2010.08.004.

[19] L.A. Bullock, M. Perez, J.G. Armstrong, J. Parnell, J. Still, J. Feldmann, Selenium and tellurium resources in Kisgruva proterozoic volcanogenic massive sulphide deposit (Norway), Ore Geol, Rev 99 (2018) 411–424, doi:10.1016/j.oregeorev.2018.06.023.

[20] A. Das, B.K. Banik, Semiconductor characteristics of tellurium and its implementations, Phys. Sci. Rev. 8 (2023) 4659–4687, doi:10.1515/psr-2021-0108.

[21] T. Rehren, J. Northover, Selenium and tellurium in ancient copper ingots, in: E. Pernicka, G.A. Wagner (Eds.), Archaeometry '90, Birkhäuser, Basel, Boston, Berlin, 1991, pp. 221–228.

[22] D. Bourgarit, B. Mille, The elemental analysis of ancient copper-based artefacts by inductively-coupled-plasma atomic-emission spectrometry: an optimized methodology reveals some secrets of the Vix crater, Meas. Sci. Technol. 14 (2003) 1538–1555, doi:10.1088/0957-0233/14/9/306.

[23] M. Cadet, T. Sayavongkhamdy, V. Souksavatdy, T. Luangkhoth, P. Dillmann, C. Cloquet, J. Vernet, P. Piccardo, N. Chang, J. Edgar, E. Foy, T.O. Pryce, Laos' central role in Southeast Asian copper exchange networks: a multi-method study of bronzes from the Vilabouly Complex, J. Archaeol. Sci. 109 (2019) 1–18, doi:10.1016/j.jas.2019.104988.

[24] M.D. Gentili, M.P. Baglione, Riflessioni su Pyrgi: scavi e ricerche nelle aree del santuario, L'Erma di Bretschneider, Roma (2013).

[25] L.M. Michetti, Caere, il suo porto e il grande santuario marittimo: nuovi dati su Pyrgi, in: F. Gilotta (Ed.), Caere 7. Lavori in Corso Su Cerveteri tra Canada ed Europa, Edizioni Consgiglio Nazionale delle Ricerche, Roma, 2023, pp. 21–36.

[26] L.M. Michetti, E. Abbondanzieri, S.S.P. Palmieri, S. Grosso, C. Tulini, C. Kourta, Tra Caere e il mare: scavi e ricerche nel comprensorio di Pyrgi (campagne 2021-2023), in: Scienze Dell'antichità, Edizioni Quasar, 2024, pp. 201–243.

[27] J. Redondo-Marugán, J. Piquero-Cilla, M.T. Doménech-Carbó, B. Ramírez-Barat, W. Al Sekhaneh, S. Capelo, A. Doménech-Carbó, Characterizing archaeological bronze corrosion products intersecting electrochemical impedance measurements with voltammetry of immobilized particles, Electrochim. Acta 246 (2017) 269–279, doi:10.1016/j.electacta.2017.05.190.

[28] F. Di Turo, Limits and perspectives of archaeometric analysis of archaeological metals: a focus on the electrochemistry for studying ancient bronze coins, J. Cult. Herit. 43 (2020) 271–281, doi:10.1016/j.culher.2019.10.006.

[29] A. Doménech-Carbó, M. Mödlinger, L. Osete-Cortina, M.T Doménech-Carbó, Mott–Schottky analysis of historical and archaeological copper–based objects, ChemElectroChem 11 (2024) 1–11, doi:10.1002/celc.202300639.

[30] M. Porcaro, M. Sanz-Abad, L.M. Michetti, A. Conti, C. De Vito, T.M. Doménech-Carbó, A. Doménech-Carbó, Correlation between voltammetry of immobilized particles and Mott-Schottky analysis of metal corrosion patinas, ChemPhysChem 26 (2025) 1–10, doi:10.1002/cphc.202400805.

[31] M.F. Alberghina, R. Barraco, M. Brai, T. Schillaci, L. Tranchina, Integrated analytical methodologies for the study of corrosion processes in archaeological bronzes, Spectrochim. Acta Part B At. Spectrosc. 66 (2011) 129–137, doi:10.1016/j.sab.2010.12.010.

[32] O. Oudbashi, A. Hasanpour, Bronze alloy production during the Iron Age of Luristan: a multianalytical study on recently discovered bronze objects, Archaeol. Anthropol. Sci 10 (2018) 1443–1458, doi:10.1007/s12520-017-0466-9.

[33] D.A. Scott, Metallography and Microstructure in Ancient and Historic Metals, Getty publications, 1992.

[34] A. Garbacz-Klempka, M. Piękoś, J. Kozana, M. Perek-Nowak, M. Wardas-Lasoń, P. Silska, M. Stróżyk, Bronze age raw material hoard from Greater Poland: archaeometallurgical study based on material research, thermodynamic analysis, and experiments, Materials 17 (2024) 2–33, doi:10.3390/ma17010230.

[35] O. Oudbashi, M. Mehofer, H. Basafa, J. Tayyari, S. Bahadori, Arsenical copper and bronze metallurgy during Late Bronze Age of north-eastern Iran: evidences from Shahrak-e Firouzeh archaeological site, Archaeol. Anthropol. Sci. 12 (2020) 1–20, doi:10.1007/s12520-020-01182-3.

[36] A. Hauptmann, S. Schmitt-Strecker, T.E. Levy, F. Begemann, On early bronze age copper bar ingots from the Southern Levant, Bull. Am. Schools Oriental Res. 373 (2015) 1–24, doi:10.5615/bullamerschoorie.373.0001.

[37] I. Segal, S.A. Rosen, Copper among the nomads: early bronze age copper objects from the camel site, central Negev, Israel, Inst. Archaeo-Metallur. Stud. 25 (2005) 3–8.

[38] K. Nagata, E. Izawa, H. Iwai, T. Watanabe, T. Nakanishi, Development of ancient copper smelting to ironmaking, ISIJ Int. 63 (2023) 2078–2085, doi:10.2355/isijinternational.ISIJINT-2023-295.

[39] G. Balassone, M. Mercurio, C. Germinario, C. Grifa, I.M. Villa, G. Di Maio, S. Scala, R. de' Gennaro, C. Petti, M.C. Del Re, A. Langella, Multi-analytical characterization and provenance identification of protohistoric metallic artefacts from Picentia-Pontecagnano and the Sarno valley sites, Campania, Italy, Measurement 128 (2018) 104–118, doi:10.1016/j.measurement.2018.06.019.

[40] M. Porcaro, F. Cognigni, M. Bernabale, G. La Penna, A. Proietti, C. Casi, C. Regoli, S. Carosi, M. Rossi, A. Brunetti, C. De Vito, Non-invasive analyses of an etruscan fibula from Vulci (Italy): the benefits of a combination of micro-raman spectroscopy, 3D reconstruction through X-ray microscopy and ED-XRF with Monte Carlo simulation, J. Raman Spectrosc. 56 (2025) 1018–1030, doi:10.1002/jrs.6834.

[41] L. Robbiola, J.-M. Blengino, C. Fiaud, Morphology and mechanisms of formation of natural patinas on archaeological Cu–Sn alloys, Corros. Sci. 40 (1998) 2083–2111, doi:10.1016/S0010-938X(98)00096-1.

[42] X. Fan, Q. Wang, Y. Wang, Non-destructive in situ Raman spectroscopic investigation of corrosion products on the bronze dagger-axes from Yujiaba site in Chongqing, China, Archaeol. Anthropol. Sci. 12 (2020) 1–10, doi:10.1007/s12520-020-01042-0.

[43] M. Ricci, F. Sebastiani, M. Becucci, M. Rogozny, V. Parfenov, A spectroscopy-based multi-analytical approach for studies in conservation: decorations in the Alexander Palace (Tsarskoye Selo), Spectrosc. J. 1 (2023) 121–136, doi:10.3390/spectroscj1030011.

[44] R.L. Frost, W. Martens, J.T. Kloprogge, P.A. Williams, Raman spectroscopy of the basic copper chloride minerals atacamite and paratacamite: implications for the study of copper, brass and bronze objects of archaeological significance, J. Raman Spectrosc. 33 (2002) 801–806, doi:10.1002/jrs.921.

[45] X.D. Liu, D.D. Meng, X.G. Zheng, M. Hagihala, Q.X. Guo, Mid-IR and raman spectral properties of clinoatacamite-structure basic copper chlorides, AMR 146–147 (2010) 1202–1205, doi:10.4028/www.scientific.net/AMR.146-147.1202.

[46] X. Zhang, I. Odnevall Wallinder, C. Leygraf, Mechanistic studies of corrosion product flaking on copper and copper-based alloys in marine environments, Corros. Sci. 85 (2014) 15–25, doi:10.1016/j.corsci.2014.03.028.

[47] A. Doménech-Carbó, M. Mödlinger, L. Osete-Cortina, M.T. Doménech-Carbó, Electrochemical approximation to bronze age chronology via multiple scan voltammetry, ChemElectroChem 10 (2023) 1–9, doi:10.1002/celc.202300405.

[48] M.T.S. Nair, L. Guerrero, O.L. Arenas, P.K. Nair, Chemically deposited copper oxide thin films: structural, optical and electrical characteristics, Appl. Surf. Sci. 150 (1999) 143–151, doi:10.1016/S0169-4332(99)00239-1.

[49] D.A. Scott, Copper compounds in metals and colorants: oxides and hydroxides, Stud. Conserv. 42 (1997) 93–100, doi:10.1179/sic.1997.42.2.93.

[50] N. Yahalom-Mack, G. Herzlinger, A. Bogdanovsky, O. Tirosh, Y. Garfinkel, S. Dugaw, O. Lipschits, Y. Erel, Combining chemical and lead isotope analyses with 3-D geometric–morphometric shape analysis: a methodological case study of socketed bronze arrowheads from the southern Levant, J. Archaeol. Sci. 118 (2020) 1–12, doi:10.1016/j.jas.2020.105147.

[51] G. Dardeniz, Chemical analysis and characterization of first millennium BC arrowheads from tarsus, PhD Thesis, Boğaziçi Üniversitesi, 2007 Yüksek Lisans Tezi.

[52] B. Constantinescu, D. Cristea-Stan, G.M. Talmatchi, D. Ceccato, New information on monetary arrowheads found in Dobroudja based on X-rays analysis of their alloy composition, in: XV, International Numismatic Congress, Taormina, 2015, pp. 332–338.

[53] M.N. Daragan, Y.N. Romanenko, Technique and technology of Scythian bronze arrowhead casting: experimental and metallographic approach, J. Archaeol. Sci. Rep. 37 (2021) 1–14, doi:10.1016/j.jasrep.2021.102919.

[54] H. Szefer, The Technology of Copper Alloys, Particularly Leaded Bronze, in Greece, its Colonies, and in Etruria during the Iron Age, Thesis, Université de Montréal, 2012.

[55] G.M. Ingo, I. Calliari, M. Dabala, G. Bultrini, T. de Caro, G. Chiozzini, Microchemical study of the corrosion products on ancient bronzes by means of glow discharge optical emission spectrometry, Surf. Interface Anal. 30 (2000) 264–268, doi:10.1002/1096-9918(200008)30:1%3C264::AID-SIA831%3E3.0.CO;2-L.

[56] V.F. Buchwald, P. Leisner, A metallurgical study of 12 prehistoric bronze objects from Denmark, J. Danish Archaeol. 9 (1990) 64–102, doi:10.1080/0108464X.1990.10590036.

[57] J.P. Pathak, S.N. Tiwari, On the mechanical and wear properties of copper-lead bearing alloys, Wear 155 (1992) 37–47, doi:10.1016/0043-1648(92)90107-J.

[58] L. Hachani, K. Zaidat, B. Saadi, X.D. Wang, Y. Fautrelle, Solidification of Sn–Pb alloys: experiments on the influence of the initial concentration, Int. J. Therm. Sci. 91 (2015) 34–48, doi:10.1016/j.ijthermalsci.2015.01.007.

[59] A. Ludwig, M. Wu, A. Kharicha, On macrosegregation, Metall. Mater. Trans. A 46A (2015) 4854–4867, doi:10.1007/s11661-015-2959-4.

[60] M. Georgakopoulou, Y. Bassiakos, O. Philaniotou, Seriphos surfaces: a study of copper slag heaps and copper sources in the context of early bronze age aegean metal production: seriphos surfaces: early bronze age aegean metal production, Archaeometry 53 (2011) 123–145, doi:10.1111/j.1475-4754.2010.00529.x.

[61] N.J. Cook, C.L. Ciobanu, T. Wagner, C.J. Stanley, Minerals of the system Bi–Te–Se–S related to the tetradymite archetype: review of classification and compositional variation, Can. Mineral. 45 (2007) 665–708, doi:10.2113/gscanmin.45.4.665.

[62] Yu.V. Seryotkin, G.A. Pal'yanova, N.E. Savva, Sulfur–selenium isomorphous substitution and morphotropic transition in the Ag3Au(Se,S)2 series, Russ. Geol. Geophys. 54 (2013) 646–651, doi:10.1016/j.rgg.2013.04.014.

[63] G. Bianchini, C. Natali, P. Ferretti, L. Casagrande, M. Conedera, C. Marchina, Trace-element distribution on sulfide mineralization in Trento Province, NE Italy, Minerals 9 (2019) 1–12, doi:10.3390/min9120736.

[64] E. Pernicka, Trace element fingerprinting of ancient copper: a guide to technology or provenance?, in: S.M.M. Young, A.M. Pollard, P. Budd, R.A. Ixer (Eds.), Metals in Antiquity, BAR International Series 792, Oxford, (1999) 163–171.

[65] Q. Wang, S. Strekopytov, B.W. Roberts, Copper ingots from a probable bronze age shipwreck off the coast of Salcombe, Devon: composition and microstructure, J. Archaeol. Sci. 97 (2018) 102–117, doi:10.1016/j.jas.2018.07.002.

[66] A.E. Josephson, The Behavior of Tellurium During Copper Ore Processing At the American Smelting and Refining Company (Tucson, AZ), University of AK Fairbanks, 2016.

[67] D. Layton-Matthews, J.M. Peter, S.D. Scott, M.I. Leybourne, Distribution, mineralogy, and geochemistry of selenium in felsic volcanic-hosted massive sulfide deposits of the Finlayson Lake District, Yukon Territory, Canada, Econ. Geol. 103 (2008) 61–88, doi:10.2113/gsecongeo.103.1.61.

[68] M. Moroni, P. Rossetti, S. Naitza, L. Magnani, G. Ruggieri, A. Aquino, P. Tartarotti, A. Franklin, E. Ferrari, D. Castelli, G. Oggiano, F. Secchi, Factors controlling hydrothermal nickel and cobalt mineralization—Some suggestions from historical ore deposits in Italy, Minerals 9 (2019), doi:10.3390/min9070429.

[69] M. Baldassarri, G. Cristoforetti, I. Fantozzi, M. Firmati, S. Legnaioli, V. Palleschi, A. Salvetti, E. Tognoni, Analisi LIBS di esemplari di AES Rude proveniente dall'abitato etrusco di Ghiaccio Forte (Scansano–GR), in: Atti Del IV Congresso Nazionale Di Archeometria, (2006) 561–573.

[70] F. Felli, G. Saviano, Studio archeometallurgico preliminare su aes rude del santuario etrusco di Pyrgi, La Metallur. Italiana 94 (2002) 43–47.

[71] G. Tanelli, I giacimenti a skarn della toscana, Rendiconti Società Italiana Di Mineralogia e Petrologia 33 (1977) 875–903.

[72] L. Chiarantini, M. Benvenuti, P. Costagliola, A. Dini, M. Firmati, S. Guideri, I.M. Villa, A. Corretti, Copper metallurgy in ancient Etruria (southern Tuscany, Italy) at the Bronze-Iron Age transition: a lead isotope provenance study, J. Archaeol. Sci. Rep. 19 (2018) 11–23, doi:10.1016/j.jasrep.2018.02.005.

[73] M. L'Héritier, S. Baron, L. Cassayre, F. Téreygeol, Bismuth behaviour during ancient processes of silver–lead production, J. Archaeol. Sci. 57 (2015) 56–68, doi:10.1016/j.jas.2015.02.002.

[74] L. Santoro, M. Boni, F. Putzolu, N. Mondillo, Base-metal sulphides and barite in the Palaeozoic of SW Sardinia: from tectonically deformed SedEx and Irish-type deposits to post-variscan hydrothermal karst and vein ores., in: Irish Association for Economic Geology, (2023) 425–439. https://doi.org/10.61153/UCNC9869

[75] D. Dungworth, An experimental study of early bronze smithing techniques, in: D. Dungworth, R.C.P. Doonan (Eds.), Accidental and Experimental Archaeometallurgy, Historical Metallurgy Society, London, 2013, pp. 149–152.

[76] M. Serghini-Idrissi, M.C. Bernard, F.Z. Harrif, S. Joiret, K. Rahmouni, A. Srhiri, H. Takenouti, V. Vivier, M. Ziani, Electrochemical and spectroscopic characterizations of patinas formed on an archaeological bronze coin, Electrochim. Acta 50 (2005) 4699–4709, doi:10.1016/j.electacta.2005.01.050.

[77] D.A. Scott, Bronze disease: a review of some chemical problems and the role of relative humidity, JAIC 29 (1990) 193–206, doi:10.1179/019713690806046064.

[78] B. Belelli Marchesini, C. Carlucci, La "fabbrica" di Pyrgi, in: Scienze Dell'antichità, Edizioni Quasar, 2022, pp. 83–104. https://www.torrossa.com/en/resources/an/5401460.

[79] S. Shalev, Y. Kahanov, C. Doherty, Nails from a 2400 year old shipwreck: a study of copper in a marine archaeological environment, JOM 51 (1999) 14–17.

[80] Y. Kahanov, N. Goltsev, S. Shalev, The copper nails from the Ma'agan Mikhael ship, Int. J. Naut. Archaeol. 30 (2001) 128–128, doi:10.1111/j.1095-9270.2001.tb01363.x.

[81] Y. Kahanov, P. Pomey, The greek sewn shipbuilding tradition and the Ma'agan Mikhael ship: a comparison with mediterranean parallels from the sixth to the fourth centuries bc, Mar. Mirror. 90 (2004) 6–28, doi:10.1080/00253359.2004.10656882.

[82] T. Dilo, N. Civici, F. Stamati, O. Cakaj, Archaeometallurgical characterization of some ancient copper and bronze artifacts from Albania, in: AIP Conference Proceedings, American Institute of Physics, 2010, pp. 985–990, doi:10.1063/1.3322596.

[83] P. Pomey, Y. Kahanov, E. Rieth, On the transition from shell to skeleton: on the transition from shell to skeleton, Int. J. Nautical Archaeol. 42 (2013) 434–438, doi:10.1111/1095-9270.12019.

[84] D.A. Scott, A review of copper chlorides and related salts in bronze corrosion and as painting pigments, Stud. Conserv. 45 (2000) 39–53, doi:10.1179/sic.2000.45.1.39.

[85] G. Bertolotti, D. Bersani, P.P. Lottici, M. Alesiani, T. Malcherek, J. Schlüter, Micro-raman study of copper hydroxychlorides and other corrosion products of bronze samples mimicking archaeological coins, Anal. Bioanal. Chem. 402 (2012) 1451–1457, doi:10.1007/s00216-011-5268-9.

[86] S.V. Krivovichev, F.C. Hawthorne, P.A. Williams, Structural complexity and crystallization: the Ostwald sequence of phases in the $Cu_2(OH)_3Cl$ system (botallackite–atacamite–clinoatacamite), Struct. Chem. 28 (2017) 153–159, doi:10.1007/s11224-016-0792-z.

[87] L.A. Battista, M. Golozar, E. Nikbin, D. Yu, M. Stanko, L. Lipcsei, J. Howe, D. Perovic, Application of scanning electron microscopy and energy-dispersive x-ray spectroscopy in the study of bronze disease on ancient copper-based artifacts, Micron 198 (2025) 1–8, doi:10.1016/j.micron.2025.103890.

[88] F. Armetta, M.L. Saladino, A. Scherillo, E. Caponetti, Microstructure and phase composition of bronze Montefortino helmets discovered Mediterranean seabed to explain an unusual corrosion, Sci. Rep. 11 (2021) 1–11, doi:10.1038/s41598-021-02425-6.

[89] M. Quaranta, E. Catelli, S. Prati, G. Sciutto, R. Mazzeo, Chinese archaeological artefacts: microstructure and corrosion behaviour of high-leaded bronzes, J. Cult. Herit. 15 (2014) 283–291, doi:10.1016/j.culher.2013.07.007.

[90] A. Petitmangin, I. Guillot, A. Chabas, S. Nowak, M. Saheb, S.C. Alfaro, C. Blanc, C. Fourdrin, P. Ausset, The complex atmospheric corrosion of $\alpha/\delta$ bronze bells in a marine environment, J. Cult. Herit. 52 (2021) 153–163, doi:10.1016/j.culher.2021.09.011.

[91] M.P Baglione, B. Belelli Marchesini, C. Carlucci, L.M. Michetti, M. Bonadies, E. Cerilli, A. Conti, B. Giuliani, M. Zinni, Pyrgi, L'area a nord del santuario: nuovi dati dalle recenti campagne di scavo, in: Scienze Dell'antichità, Edizioni Quasar, 2017, pp. 149–194.

[92] O. Oudbashi, A. Hasanpour, P. Davami, Investigation on corrosion stratigraphy and morphology in some Iron age bronze alloys vessels by OM, XRD and SEM–EDS methods, Appl. Phys. A 122 (2016) 262, doi:10.1007/s00339-016-9793-4.

[93] L. Robbiola, R. Portier, A global approach to the authentication of ancient bronzes based on the characterization of the alloy–patina–environment system, J. Cult. Herit. 7 (2006) 1–12, doi:10.1016/j.culher.2005.11.001.

[94] M. Quaranta, On the degradation mechanisms under the influence of pedological factors through the study of archeological bronze patina, PhD Thesis, Alma Mater Studiorum Università di Bologna, 2009.

[95] F. Boccaccini, C. Riccucci, E. Messina, M. Pascucci, F. Bosi, D. Chelazzi, T. Guaragnone, P. Baglioni, G.M. Ingo, G.D. Carlo, Reproducing bronze archaeological patinas through intentional burial: a comparison between short- and long-term interactions with soil, Heliyon 9 (2023) 1–13, doi:10.1016/j.heliyon.2023.e19626.

[96] M.J. Hutchison, J.R. Scully, Patina enrichment with SnO2 and its effect on soluble Cu cation release and passivity of high-purity Cu-Sn bronze in artificial perspiration, Electrochim. Acta 283 (2018) 806–817, doi:10.1016/j.electacta.2018.06.125.

[97] C. Chiavari, K. Rahmouni, H. Takenouti, S. Joiret, P. Vermaut, L. Robbiola, Composition and electrochemical properties of natural patinas of outdoor bronze monuments, Electrochim. Acta 52 (2007) 7760–7769, doi:10.1016/j.electacta.2006.12.053.

[98] F. Ospitali, C. Chiavari, C. Martini, E. Bernardi, F. Passarini, L. Robbiola, The characterization of Sn-based corrosion products in ancient bronzes: a Raman approach, J. Raman Spectrosc. 43 (2012) 1596–1603, doi:10.1002/jrs.4037.

[99] L. Robbiola, C. Fiaud, A. Harch, Characterisation of passive layers of bronze patinas (Cu-Sn alloys) in relation with the tin content of the alloy, in: The Institute of Materials, Parigi, (1993) 150–154. https://hal.science/hal-00975715v1

[100] L. Robbiola, T.T.M. Tran, P. Dubot, O. Majerus, K. Rahmouni, Characterisation of anodic layers on Cu–10Sn bronze (RDE) in aerated NaCl solution, Corros. Sci. 50 (2008) 2205–2215, doi:10.1016/j.corsci.2008.06.003.

[101] D.A. Scott, Copper and Bronze in Art: Corrosion, Colorants, Conservation, Getty publications, Los Angeles, 2002.